Evaluating the Time-Dependent Melting Behavior of Semicrystalline Polymers Through Strobl's 3-Phase Model

Jonathan Dan Hoang

Thesis submitted to the faculty of the Virginia Polytechnic Institute and State University in partial fulfillment of the requirements for the degree of

Master of Science
In
Materials Science and Engineering

Hervé Marand
Sean G. Corcoran
Abby R. Whittington

13 February 2013
Blacksburg, VA

Keywords: polymer crystallization, melting, Lauritzen-Hoffman secondary nucleation theory, Strobl 3-Phase model, isotactic polystyrene

Evaluating the Time-Dependent Melting Behavior of Semicrystalline Polymers Through Strobl's 3-Phase Model

Jonathan Hoang

ABSTRACT

The melting behavior of polymers can provide information on their crystallization mechanism. However, the origin of the time-dependent low endotherm, or annealing peak, and the extent of melting-recrystallization-remelting during heating are still debated. The crystallization and subsequent melting behavior of isotactic polystyrene are explored in the context of Strobl's 3-Phase model using differential scanning calorimetry (DSC), small angle X-ray scattering (SAXS), and wide angle X-ray diffraction. DSC experiments confirm the existence of a crystallization time-dependent low endotherm, and melting-recrystallization-remelting processes during heating. SAXS analysis using the correlation function confirms that the lamellar thickness increases with crystallization temperature and is independent of time. The spread between equilibrium melting and crystallization temperatures determined in this work (T_f^∞ = 533K, T_c^∞ = 544K) is much smaller than reported by Strobl et al. (T_f^∞ = 562K, T_c^∞ = 598K). These differences are partially attributed to overestimation in lamellar thicknesses calculated through the interface distribution function. Analysis of diffraction broadening shows that the apparent crystal size decreases with crystallization time, suggesting the formation of smaller/less perfect crystals during secondary crystallization. These results are consistent with observations that the glass transition temperature increases with crystallization time and supports the idea that secondary crystallization leads to increased amorphous conformational constraints. These results also suggest that the upward shift of the annealing peak during secondary crystallization is associated with increased amorphous

constraints rather than increased crystal dimensions. The lack of distinction between T_f^{∞} and T_c^{∞} and the evolution of crystal size during crystallization stand in direct contrast with Strobl's model.

Acknowledgements

It is cliché to me to note that I would not be here without the support and guidance of several individuals, but I will go ahead nonetheless. I first need to thank my wife, Amanda, for being willing to uproot her life from what she had enjoyed doing and wanted to be for so long. I know this has been such an incredible sacrifice, but I will be forever thankful to have you by my side during this adventure. I know that whatever life has in store for us next, it will be a blessing because I get to share it with you. You have shown me that whenever I have felt down and out with this whole process, I still have a lot more to give. Along with this, I would like to thank my parents. Without my dad, the cross-country gauntlet we did to get me out here would not have been bearable, let alone possible. Driving 2300 miles in 55 hours would have been a disaster, and my mom, for letting us run ourselves to the bone like that. But seriously, without them instilling the drive I have to learn, I would not be here working on a second master's degree, while also knowing that with a lot of hard work, determination, and goals, I would never had tried to better myself.

I am incredibly indebted to Dr. Hervé Marand. By first letting me join his research group and then helping me every step along the way so I could finish this program, I am incredibly thankful. I have learned more than I could have imagined throughout this process and extremely appreciative for him taking the time to teach and work with me. His insight and input have greatly aided my cave-man approach towards solving problems and helped me realize a more critical way to approach the work I whole-heartedly love.

I owe Swapnil Sheth, my colleague from the Marand group, immense thanks for taking the time to teach me how to operate all of the instrumentation and having someone to talk about research with.

Akin to that, I owe sincere thanks to Dr. Robert Moore and Mingquing Zhang from his research group for allowing me to use their SAXS (of course under supervision!). With that being a great portion of my work, I'd be done either a lot sooner and/or have a lot less to talk and think about without their help.

Of course, the MSE department for admitting me into the graduate program. Within the department, I owe great thanks to Dr. Robert Hendricks for answering the questions I had regarding processing my XRD data. Without his help, I'd still be sitting and scratching my head trying to understand what to do with my diffraction patterns. Although things did not quite work out, I hope the work is paved for future students to use the Warren-Averbach method in the Marand group.

I owe immense thanks to the United States Air Force for selecting me for a graduate school assignment. I would like to note though the views expressed in this work are those of the author and do not reflect the official policy or position of the United States Air Force, Department of Defense, or the U.S. Government.

To all of the friends Amanda and I made while here, you made this opportunity enjoyable and pleasant.

Last, I would ultimately like to thank the Big Man for allowing me to have found something to be passionate about and opening the doors to allow me to pursue these dreams and interests that You have filled me with. You have blessed me repeatedly and made me lucky beyond measure.

Dedication:

My wife, Amanda, for being so boss, she should be the one at the end of World 8-4, while also being so sweet, Slugworth would want to steal her, instead of Wonka's everlasting gobstopper. Also, God, through which all of this would not have been possible, continuing to give me strength that I could ever figure of this out, let alone finish.

Table of Contents

Page

List of Figures

List of Tables

CHAPTER 1: INTRODUCTION

Bulk polymer crystallization in the absence of stress or strain involves the formation of primary crystal nuclei and the subsequent growth of crystalline lamellae. The radial three-dimensional growth of these lamellae from the primary nucleus leads to the formation of spherulites.[1] In experiments on solution-grown polyethylene lamellae, Keller observed that the lamellar thickness is much smaller than the actual chain length and that the chain axis is approximately perpendicular to the basal planes of the lamellae. This led him to conclude that flexible polymer chains crystallize through a chain folding mechanism.[2] Polymer lamellae have since been demonstrated to form during bulk crystallization from the melt, with the chain folding mechanism being confirmed as well.[3-6]

Although the chain-folded nature of crystalline polymer lamellae is well understood, there is still much debate as to mechanism of their formation and the nature of their melting behavior. Examination of the literature indicates that two different theories are invoked in discussions of polymer crystallization: the Secondary Surface Nucleation theory by Lauritzen and Hoffman[7] (LH) and the 3-Phase model by Strobl.[8] The LH model predicts that the formation of polymer lamellae is controlled by secondary nucleation of polymer stems on the crystal growth front.[7] The LH model assumes that the melt-to-crystal phase transformation during chain folding establishes the thickness and other structural characteristics of crystal lamellae. As a result of its intuitive nature and mathematical tractability, it has been widely applied in the analysis of crystallization data. However, the LH model is not without controversy, due in part to difficulties in making physical sense of the different crystallization regimes in obtaining independent

confirmation of its predictions. Furthermore, the LH model does not shed light on the structural evolution of lamellar crystals after their formation. This has led to formulation of new theoretical treatments over the years, although the LH theory persists. Most recently, Strobl's Three-Phase model[8] has gained some attention as an alternate model of polymer crystallization. Strobl[8] postulates that amorphous polymer chains begin to order and transform to a mesomorphic phase when in the direct vicinity of the crystal growth front. With time the mesomorphic phase thickens in the direction parallel to the chain axis and eventually undergoes a stabilization process leading to the formation of three-dimensional crystal blocks, or grains. These blocks then increase in perfection and merge with other blocks to form polymer lamellae. Strobl[8] postulates that the growth rate of polymer lamellae is dictated by the amorphous-mesomorphic transition, while their thickness is controlled by the process the three-dimensional grains undergo in forming lamellae.[8]

In the context of the aforementioned polymer crystallization theories, the focal point of this work is to gain a better understanding of the dependence of the melting behavior of semicrystalline polymers on crystallization time. Strobl's 3-Phase model of polymer crystallization is evaluated to discern whether it can provide an adequate explanation for the change in the observed melting behavior with crystallization time. This is explored further in Chapter 2. Several factors have led us to select isotactic polystyrene (it-PS) as the polymer of choice for this work. First, the crystal growth rate of this polymer is slow compared to other semicrystalline polymers due, in part, to the bulky phenyl side groups and the associated chain stiffness, which are thought to reduce the rate of chain folding. Additionally, any changes to the morphology are inhibited when the

polymer is quenched from the melt or crystallization temperature to room temperature, due to the high glass transition temperature (T_g ~ 100°C). This eases the processing of samples for the structural and thermodynamic analyses performed in this work. Last, it is a flexible chain polymer, which would lead to the notion that chain folding occurs in the development of polymer lamellae. The following figure is a representation of polystyrene.

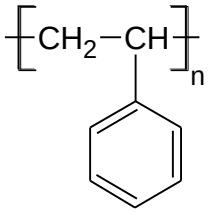

Figure 1.1 – Polystyrene repeat unit

In chapter 2, we will discuss the background literature related to this project. In chapter 3, we will describe the material and the experimental techniques used in this study. Chapter 4 will focus on the actual methods of analysis and chapter 5 on the results, their interpretation and the discussion. Finally, the last chapter of this thesis will bring us to some elaboration on the recommended future work.

CHAPTER 2: BACKGROUND

2.1 Polymer Crystallization Theories

As previously mentioned, the two theories on polymer crystallization discussed in this work are the Lauritzen-Hoffman secondary nucleation theory[7] and Strobl's Three-Phase model.[8] In the following sections, the two theories are explored in further detail.

2.1.1 Lauritzen-Hoffman Theory

Since its first iteration in 1961, the Lauritzen-Hoffman theory[7] of polymer crystallization has received multiple revisions. Despite these changes, the polymer crystallization mechanism postulated in this theory has remained the same. It considers that the growth of polymer lamellae is controlled by secondary nucleation of polymer chains at the crystal growth front. For the sake of mathematical tractability the model is not concerned with the evolution of the lamella subsequent to its formation. The model for bulk crystallization can be seen in the following figure.

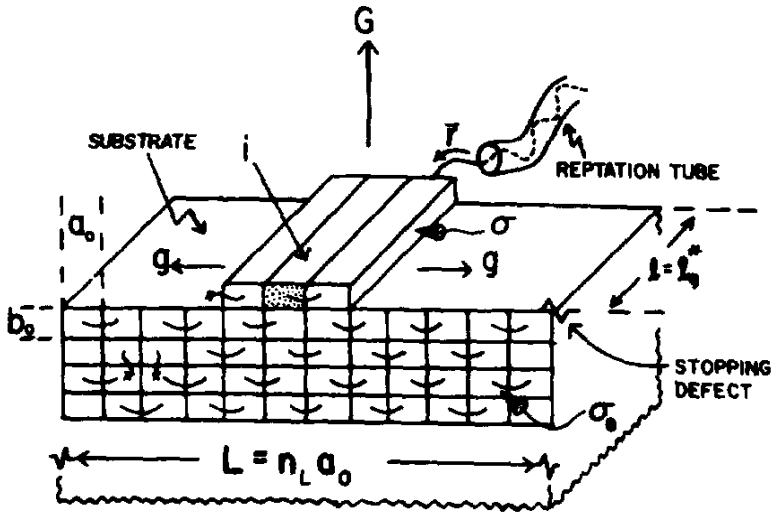

G=crystal growth rate
r=reeling in rate
l=lamellar thickness
i=secondary nucleation rate
g=substrate completion rate
a_o=stem width
b_o=stem thickness
σ=lateral surface free energy
σ_e=fold surface free energy

Figure 2.1 - Schematic of the crystal growth front in the LH crystallization model[9]

In the context of the LH model, polymer crystallization can occur under any of three regimes: Regimes I, II, and III. Qualitatively, the difference between the three regimes originates from the relative rates of secondary nucleation and substrate completion through chain folding. In regime I, which occurs at low undercooling, secondary nucleation is a rare event. In this regime, when a stem nucleates on the growth front, it spreads across the substrate by chain folding and creates a new crystal layer. In regime II, which occurs at higher supercoolings, secondary nucleation occurs more frequently, and multiple stems nucleate onto the crystal growth face concurrently. The formation of a new layer occurs through competition between nucleation and substrate completion. The transition between regimes I and II occurs when the nucleation rate is equal to

$$i = \frac{2g}{L^2} \tag{2.1}$$

In regime III, the secondary nucleation rate is so fast that that lateral spreading through chain folding does not contribute significantly to layer completion or crystal growth. The transition between regimes II and III occurs when the nucleation rate is given by

$$i = \frac{2g}{(n_{III}a_o)^2} \tag{2.2}$$

A schematic of the growth front in the different regimes is shown below in Figure 2.2.

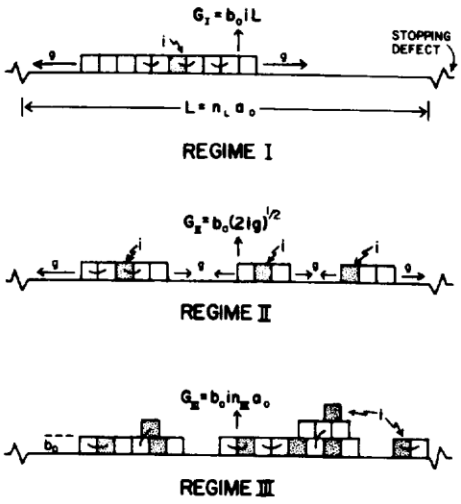

Figure 2.2 – Schematic of the growth fronts in regimes I, II and III according to the LH theory[9]

As predicted by the LH theory, the initial lamellar thickness for a particular crystallization temperature is given by

$$l_g^* = \frac{2\sigma_e}{(\Delta G)} + \delta l \tag{2.3}$$

Where the first term is the minimum thickness that is stable at the crystallization temperature (ΔG is the free energy of fusion at that temperature) and is offset by some additional term, given by

$$\delta l = \frac{kT}{2b_0\sigma}\left[\frac{2+(1-2\psi)a_o\frac{\Delta G}{2\sigma}}{\left(1-\frac{a_o\psi\Delta G}{2\sigma}\right)*\left(1+\frac{a_o(1-\psi)\Delta G}{2\sigma}\right)}\right] \tag{2.4}$$

where ψ, the apportionment factor, is a number between 0 and 1, which describes the fraction of units of the crystallizing stem that have a truly crystalline character. Without the second term in 2.4, the crystal would melt its own crystallization temperature, which obviously is not observed experimentally.[10] This idea caused significant debate early on when the LH theory was introduced. For crystallization at high supercooling, a divergence arises in 2.4, suggesting that infinitely thick polymer lamellae would exist

when the apportionment factor, was equal to 1. [9,11] Again, this is not observed experimentally and Hoffman et al. [9,12] later showed that the value of ψ is low, hence removing the controversy associated with the δl catastrophe.

For this mechanism of secondary nucleation, the driving force is the lowering of the free energy of the nucleus through chain folding. The free energy change associated with the deposition of the first stem and subsequent stems are given respectively in equations 2.5 and 2.6

$$\Delta\emptyset_v = \left(2b_o l\sigma + 2a_o b_o \sigma_e - a_o b_o l(\Delta G)\right) \tag{2.5}$$

$$\Delta\emptyset_v = (2b_o l\sigma - a_o b_o l(\Delta G)) - (v-1)(a_o b_o l(\Delta G) - 2a_o b_o \sigma_e) \tag{2.6}$$

The cascading effect of stem attachment and decreasing free energy can be seen below.

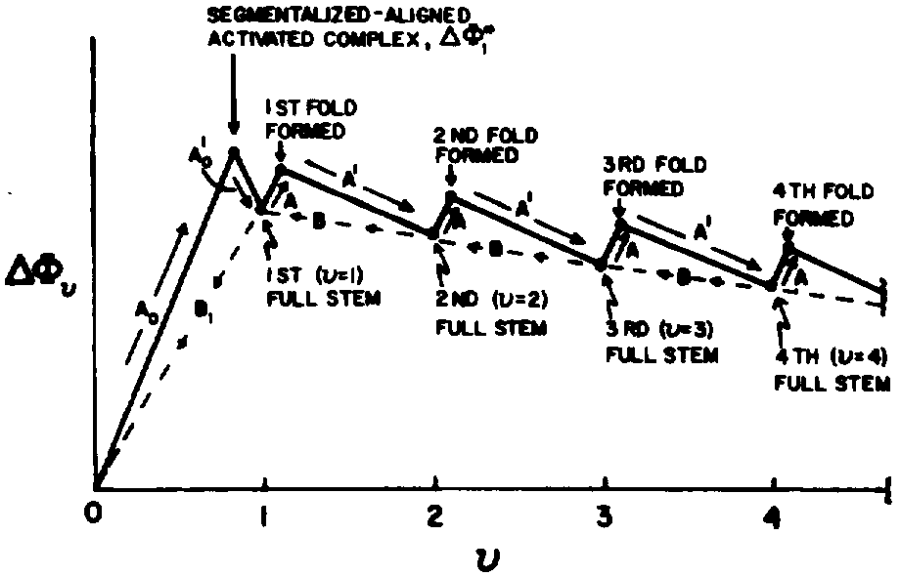

Figure 2.3 - Free energy diagram: nucleus free energy vs. number of crystalline stems[9]

The terms A_0, A', and B represent rate constants for the first stem deposition on the substrate, and for subsequent stem attachment and detachment from the substrate, respectively.[9] The LH theory of polymer crystallization considers only two phases, the

crystal and melt, which stands in significant contrast to the model proposed by Strobl. One should also note that the LH theory is only concerned with the crystal growth rate and the initial lamellar thickness characteristic of primary crystallization. Hence, it does not address any of the processes that may take place behind the growth front, such as lamellar thickening, formation of subsidiary lamellae or secondary crystals, etc…

2.1.2 Strobl Three-Phase Model

Strobl's model[8] approaches bulk crystallization from a different perspective. Instead of chains spreading on the substrate through a folding mechanism, Strobl proposes a three-step transformation process. Each subsequent step results in greater ordering of the polymer chains, and therefore stability of the structure. This process is illustrated in the following figure.

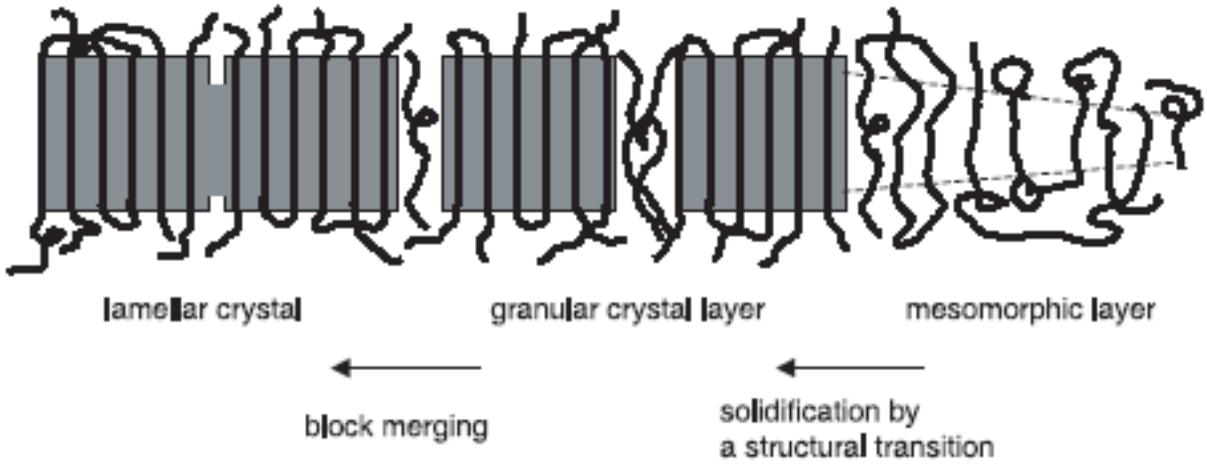

Figure 2.4 - Strobl's 3-Phase model[8]

The growth front of the crystal is located at the interface of the amorphous and mesomorphic regions. Chains in the growth front are not considered crystalline. As amorphous polymer chains feel the vicinity of the growth front, they develop a mesomorphic character. With time, chains in the mesomorphic layer acquire three-

dimensional order as they crystallize in the form of a granular or native crystal. A surface ordering process occurs along the surfaces of the native crystals to form stabilized crystals, or the familiar polymer lamellae. Strobl labels this event as solidification by structural transition, as seen in the above figure. Strobl proposes that the crystal blocks increase in perfection as they merge to form a more stable lamella. According to Strobl et al.[11] the crystalline blocks are observed as the granular regions in the following atomic force microscope image.

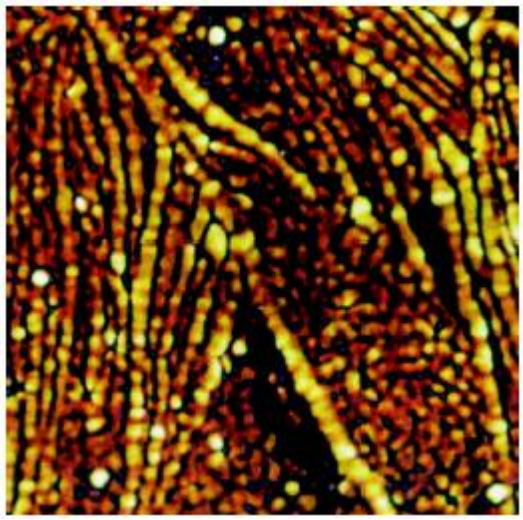

Figure 2.5 – AFM image obtained in tapping mode for syndiotactic polypropylene[11]

Similar observations have been reported in select scanning and tunneling electron microscope images as well. In Strobl's treatment, the thickness of the lamellae is established at the stage of formation of the granular blocks and does not vary with crystallization time, as determined by small angle X-ray scattering (SAXS) experiments. Hence, the lamellar thickness is controlled by the undercooling below the mesomorph-to-native crystal transition temperature. In contrast, the crystal growth rate is controlled by events occurring at the interface between the amorphous and mesomorph layers, hence by the undercooling below the amorphous-to-mesomorph transition temperature.[11,13]

Strobl developed his three-phase model through inferences drawn from work performed by Keller et al.[14] and from Imai et al.[16] The former noted the during crystallization of poly(ethylene-co-octene) under high pressure, a hexagonal (disordered) polymorph was initially observed, which transformed upon cooling into the more stable orthorhombic phase. Keller postulated that the disordered phase could also form at ambient pressures, but was only stable on the nanometer scale.[14] Keller et al.[14] further proposed that such crystallization process was an example of Ostwald ripening, which states that crystal growth proceeds through the crystal phase that exhibits the lowest surface free energy structure.[11,15] On the basis of scattering experiments, Imai et al.[16] speculated that the actual crystallization of polymers always occurs through some non-crystalline precursor phase.

Much information in Strobl's theory is related to two characteristic curves, the crystallization and melting lines.[8,11] These two lines are the physical manifestation of his three-phase model. The crystallization line is obtained by plotting the crystallization temperature as a function of the inverse lamellar thickness, while the melting line represents the melting temperature as a function of inverse lamellar thickness. The melting temperature can be obtained either from differential scanning calorimetry (DSC) data or from SAXS experiments, while the lamellar thickness is typically calculated from SAXS data. A typical plot of melting and crystallization lines can be seen in the following figure, in the case of isotactic polystyrene using a 0.2°C/min heating rate to record the melting temperature using SAXS.

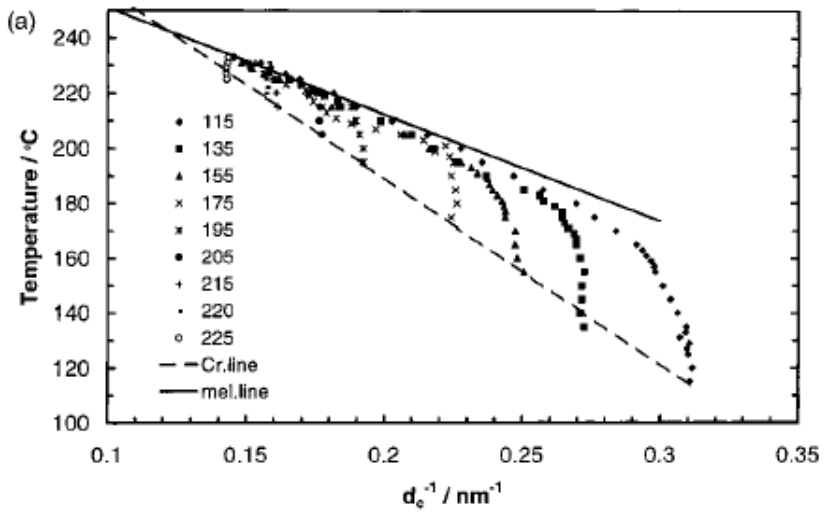

Figure 2.6 – Temperature vs. reciprocal of lamellar thickness during heating subsequent to isothermal crystallization of it-PS[17]

When these curves are linearly extrapolated to a crystal of infinite thickness ($1/d_c = 0$), the Gibbs-Thomson relation gives the equilibrium melting temperature (T_m^{∞}), while the crystallization line yields an equilibrium crystallization temperature, which Strobl labels the characteristic temperature, T_c^{∞}.[11] In order to study crystallization at higher temperatures, and ultimately thicker crystals, Strobl employs a self-seeding method, followed by isothermal crystallization. Self-seeding is a process that promotes crystallization by lowering the free energy barrier by creating surfaces [nuclei] for crystallization to occur. The following figure shows experimental results for a syndiotactic poly(propylene-co-octene) sample containing 20% octene (sPPcO20). The open squares represent the lamellar thickness data for samples crystallized using self-seeding, while the open circles represent lamellar thickness data obtained during lower temperature crystallization without self-seeding. Note that to define the characteristic temperature, T_c^{∞}, the linear extrapolation of the crystallization line omits the data obtained by self-seeding.

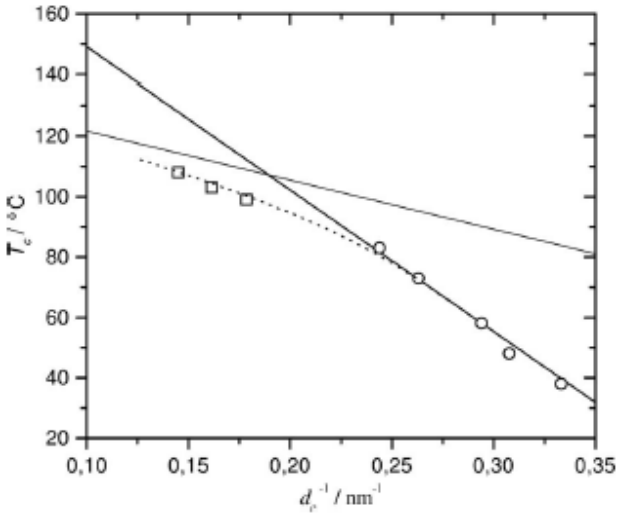

Figure 2.7 – Temperature vs. reciprocal of lamellar thickness during isothermal crystallization of sPPcO20[11]

To address the issue of lamellar thickening during heating, crystallization experiments were performed at various temperatures by Heck et al.[18] Temperature dependent SAXS experiments were performed by heating a sample up to its melting temperature and measuring its lamellar thicknesses as a function of temperature during heating. Such experiments showed that the lamellar thickness, while independent of crystallization time, varies with temperature during heating above the crystallization temperature. Plots of T vs. $1/d_c$ during heating exhibit a linear stage, with a slope intermediate between that of the melting and crystallization lines. Since this line extrapolates to the same characteristic temperature as the crystallization line, it has been denoted as the recrystallization line by Strobl.[18] Unlike the crystallization and melting lines, the recrystallization line is dependent on the crystallization and heating conditions used. The following figure depicts the crystallization, recrystallization, and melting lines for sPPcO20.

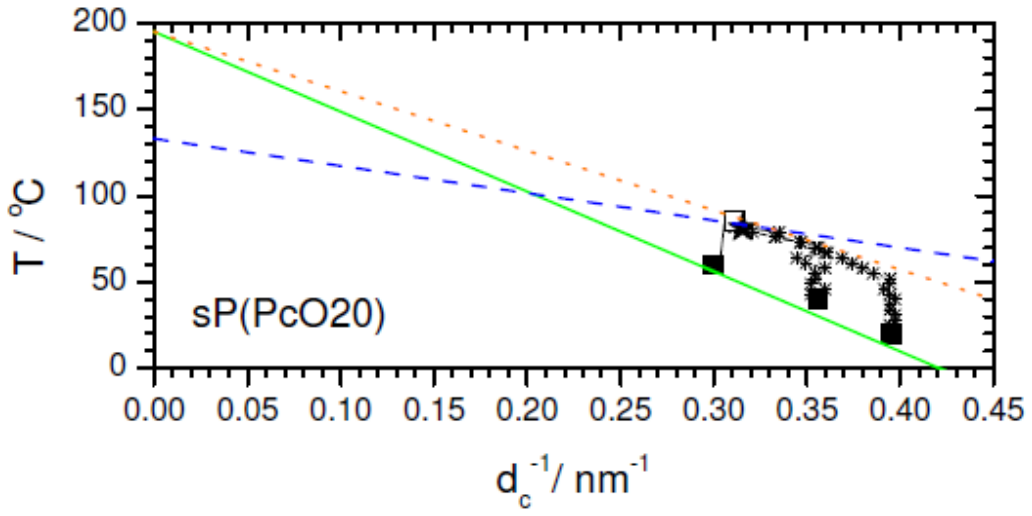

Figure 2.8 – Crystallization (full), recrystallization (dotted), and melting (dashed) lines for sPPcO[18]

In summary, Strobl suggests that the three characteristic temperatures (the equilibrium crystallization temperature (T_c^∞), the equilibrium fusion temperatures (T_f^∞) and the zero growth temperature (T_{zg})) are identical with the three equilibrium transition temperatures associated with the three possible phase transitions between the amorphous, mesomorphic and crystal phases, namely the mesomorph-crystal transition temperature (T_{mc}^∞), the amorphous-crystal transition temperature (T_{ac}^∞), and the amorphous-mesomorph transition temperature (T_{am}^∞). Beginning with the lowest of the transition temperatures, T_{am}^∞ governs the transition between the amorphous and mesomorphic state. Since crystal growth is initiated by a transformation from the amorphous to the mesomorphic state, crystal growth is inhibited at T_{zg}. The next transition temperature, T_{ac}^∞, deals with the transition from the crystal to the amorphous or melt state. No crystalline lamella can be observed above this temperature. However, as noted earlier, two morphological states are proposed for the crystal phase by Strobl, namely the native and the stable crystals. Therefore, $T_{ac_s}^\infty$ experimentally corresponds to the melting line.

Last, the T_{mc}^{∞} governs the transition between the mesomorphic to the crystalline state. Again, since there are two populations of crystals, we need to distinguish $T_{mc_n}^{\infty}$ and $T_{mc_s}^{\infty}$, which define the crystallization and recrystallization lines, respectively. In contrast to the LH model, Strobl argues that the lamellar thickness is governed by the degree of supercooling below T_c^{∞} instead of T_f^{∞}. In the same fashion that one typically writes the Gibbs-Thomson equation (see below), we can write similar relationships for the size dependence of the mesomorph-crystal (native or stabilized) and mesomorph-amorphous transition temperatures.

The traditional Gibbs-Thomson equation is written as

$$T_f = T_f^{\infty}\left(1 - \frac{2\sigma_e}{\rho_c d_c \Delta H_{fus}}\right) \tag{2.7}$$

where σ_e is the fold surface free energy, ρ_c is the crystal density, d_c is the crystal thickness, and ΔH_{fus} is the specific heat of fusion. The Gibbs-Thomson analogues for the crystallization and recrystallization lines are given, respectively, by:

$$T_c^{\infty} - T \approx \frac{(2\sigma_{ac_n} - 2\sigma_{am})T_c^{\infty}}{\Delta h_{cm}}\frac{1}{n} \tag{2.8}$$

$$T_c^{\infty} - T \approx \frac{(2\sigma_{ac_s} - 2\sigma_{am})T_c^{\infty}}{\Delta h_{cm}}\frac{1}{n} \tag{2.9}$$

Similarly for the amorphous-mesomorph transition, one can write:

$$T_{am}^{\infty} - T \approx \frac{2\sigma_{am}T_{am}^{\infty}}{\Delta h_{am}}\frac{1}{n} \tag{2.10}$$

where $\sigma_{ac_s} = \sigma_e$, the free energy of the stabilized crystal and n, the number of monomer units in a stem, given by $d_c/\Delta z$ and Δz is the length per monomer unit. Assuming linear behavior for all three curves, Strobl[8] constructs a "nanophase diagram", which is seen in the following figure.

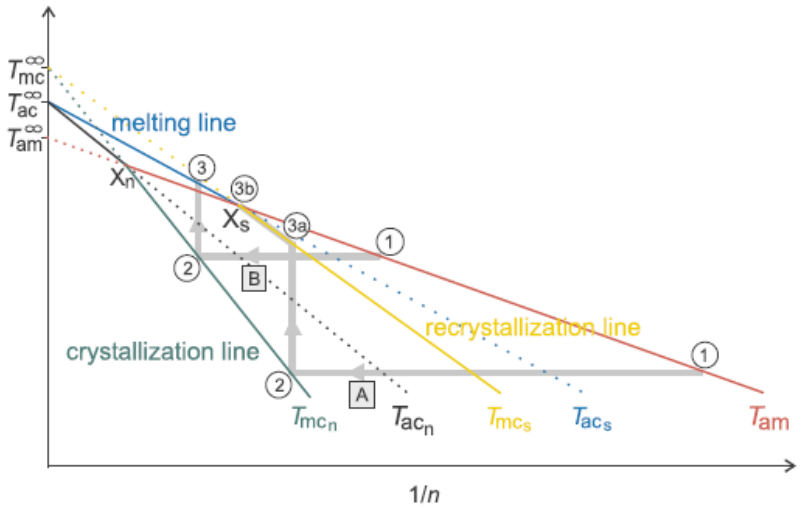

Figure 2.9 – Nanophase diagram[8]

Two points are of particular significance in Figure 2.9, namely the triple points given by X_s and X_n. These are explained in the following thermodynamic treatment. He begins by expressing the difference in Gibbs free energy between the crystal and the amorphous phases and between the mesomorph-amorphous as:

$$\Delta g_{ac} = g_c - g_a \tag{2.11}$$

$$\Delta g_{am} = g_m - g_a \tag{2.12}$$

Assuming, as a first approximation, a linear temperature dependence for each free energy change leads to the following plot:

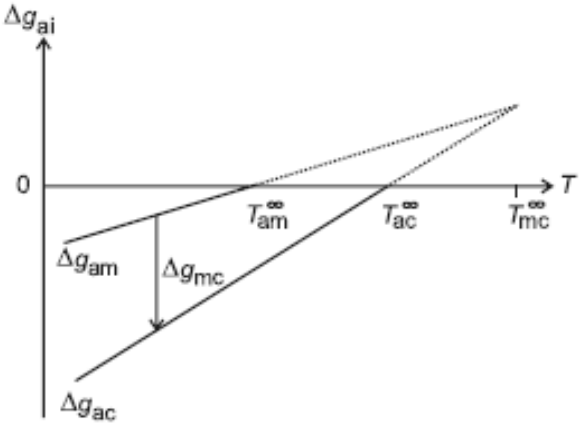

Figure 2.10 – Δg for polymer crystallization[13]

One should note, first, that the corresponding entropy changes, ΔS_{ac} and ΔS_{am}, are the slopes of the Δg_{ai} lines in Figure 2.10 and, second, that the inequality $\Delta S_{ac} > \Delta S_{am}$ must be satisfied, considering the nature of the crystal, mesomorph and amorphous phases. Indeed, the crystal phase exhibits the lowest entropy of the three, while the amorphous phase exhibits the largest. Such constraints lead to the inequality $T_{am}^{\infty} < T_{ac}^{\infty} < T_{mc}^{\infty}$. From Figure 2.10, we can also conclude the following relationship between the enthalpy changes for the amorphous to mesomorph and amorphous to crystal transformations.

$$\frac{\Delta h_{am}}{\Delta h_{ac}} = \frac{\Delta s_{am} T_{am}^{\infty}}{\Delta s_{ac} T_{ac}^{\infty}} \approx \frac{(T_{mc}^{\infty} - T_{ac}^{\infty}) T_{am}^{\infty}}{(T_{mc}^{\infty} - T_{am}^{\infty}) T_{ac}^{\infty}} \tag{2.13}$$

While the thermodynamic concepts discussed by Strobl[8] apparently explain the various nanophase diagrams recorded to date, it should be noted that no direct evidence has been given for the existence of the mesomorph.

2.2 Secondary Crystallization

Before delving into the concept of secondary crystallization, it is necessary to discuss primary crystallization. In the traditional sense, the crystallization process can be described by Avrami equation, as seen below

$$X_c(t) = X_c^{\infty}(1 - e^{-Kt^n}) \tag{2.14}$$

The term $X_c(t)$ gives the volume fraction of crystalline material at crystallization time, *t*. X_c^{∞} is the limiting volume fraction of crystallinity for a spherulite at the end of primary crystallization. Finally, K and n are constants used to describe the geometry of crystal growth (one, two, or three-dimensional) and the nature of the primary nucleation process (athermal, random, or mixed).[26] The Avrami equation is only useful in describing the crystallinity evolution while the linear growth rate is constant. This is only the case until the polymer spherulites impinge with one another. At this point, primary crystallization is

complete, and secondary crystallization takes over. The following figure demonstrates the impingement of polymer spherulites.

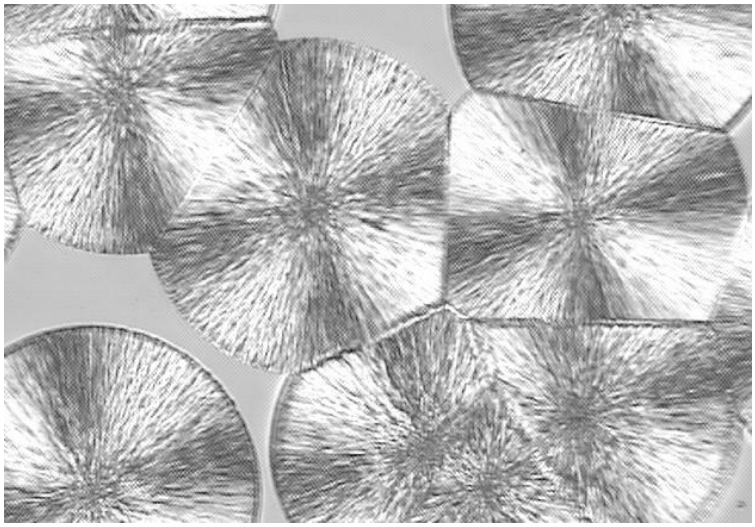

Figure 2.11 – Polarized optical micrograph of impinging it-PS spherulites

Additionally, secondary crystallization is confirmed by DSC experiments, which show the crystallinity continuing to increase once the primary crystallization is complete. The following figure is an Avrami curve generated using DSC data for linear polyethylene. On this figure, contributions to the degree of crystallinity from primary and secondary crystallization are separated.[19] Under these experimental conditions, the secondary crystallization stage appears to begin after about 10 min, when the degree of crystallinity arising from primary crystallization reaches approximately 40%.

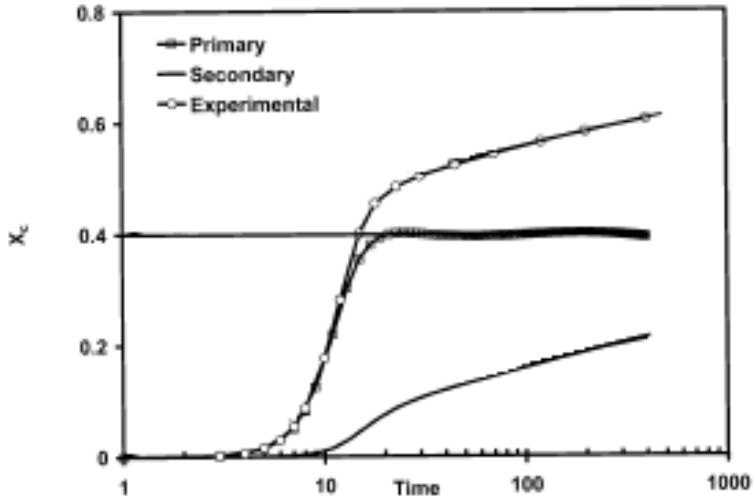

Figure 2.12-Evolution of primary and secondary crystallinity with crystallization time at T_x = 127°C for linear poly(ethylene)[19]

Secondary crystallization encompasses three possible mechanisms, which may occur in any combination.

First, secondary crystallization can take place through the nucleation and growth of new polymer crystals, in the amorphous regions between polymer lamella formed during the primary crystallization process. Hsiao et al.[20] attributed the decrease in long period and lamellar thickness with increased isothermal crystallization time for poly(butylene terephthalate) to the formation of secondary crystals between primary lamellae. Hild et al.[21] performed wide-angle X-ray diffraction (WAXD) experiments on low isotactic poly(propylene) to demonstrate the formation of secondary lamellae. Hild associated the formation of primary lamellae to polymer chains of high isotactic content, and the formation of secondary lamellae to chains of lower tacticity, which were initially rejected during primary crystallization. Without going into specifics, Strobl predicts the low melting-endotherm observed in DSC experiments is attributed to the secondary crystals formed during the crystallization process.[17]

The second mechanism of secondary crystallization is the isothermal lamellar thickening process. This process is driven by the minimization of the surface to volume ratio of thin polymer lamellae. Thickening indeed increases the thermal stability of polymer lamellae. Early SAXS experiments by Hoffman and Weeks showed an increase in lamellar thickness for poly(ethylene) with increased isothermal crystallization time.[22] Marand and Huang have shown that the lamellar thickening of primary polyethylene crystals observed through SAXS studies is consistent with the change in melting temperature with time observed in DSC experiments.[19]

A third mechanism of secondary crystallization is associated with the increase in the lateral dimensions of polymer crystals. In the context of Strobl's model,[8] this can also be viewed as an increase in crystal perfection. Indeed the merging of mesomorphic boundaries between crystal blocks is expected to give rise to an increase in crystal size and crystallinity. Polymer lamellae may also undergo an increase in crystalline perfection, through reduction of strain in the fold surfaces, induced during primary crystallization by the chain-folding process, and the non-ideal packing of stems in the primary polymer crystals.[23] Using wide-angle X-ray diffraction, dilatometry, and DSC experiments, Alfonso et al.[24] showed a systematic increase in crystal dimensions and bulk density and the upward shift of the low melting endotherm with crystallization time subsequent to primary crystallization. However, since the peak broadening observed in the WAXD experiments was analyzed using the Debye-Scherrer equation the authors could not separate effects associated with associated with increased lateral dimensions from effects associated with a decrease in lattice strain. Di Lorenzo et al.[25] used temperature modulated DSC (TMDSC) to study reversible and irreversible melting in

poly(amide-block-ether)s. The irreversible melting observed was attributed to primary and secondary crystallization and increased perfection of the polymer crystals. Strobl indicates that except for linear polyethylene and a few other flexible polymers, which exhibit a crystal alpha relaxation process and sufficient chain mobility in the crystal phase, most homopolymers and random copolymers do not exhibit the mechanism of lamellar thickening. Strobl also suggests that secondary crystal formation is a common mechanism of secondary crystallization. In contrast to Hsiao et al.[20] Strobl suggests that secondary crystals exhibit the same lamellar thickness as primary crystals. We now turn our attention to the evolution of the melting temperature of crystals as a result of secondary crystallization.

2.3 Relation to Current Work

The focus of this work is to evaluate the time-dependent melting behavior of semicrystalline polymers in the context of Strobl's 3-Phase Model. Strobl's 3-Phase model argues that the upward shift of the low melting endotherm observed with increased crystallization time in DSC experiments cannot be attributed to a lamellar thickening mechanism. Furthermore, Strobl acknowledges that at high supercoolings, the crystallization process is riddled with crystal defects. Hence, with an increase in crystallization time, secondary crystallization should involve an increase in perfection of the nascent crystals.[11,17] Indeed, temperature dependent SAXS experiments performed on it-PS demonstrate that a change in lamellar thickness does not occur during isothermal crystallization and is only observed above the initial crystallization temperature.[17] It has been documented that annealing other bulk semicrystalline polymeric materials above their initial crystallization temperature will result in an increase in lamellar thickness.[26] It

is worthwhile to note that if there is no observed increase in lamellar thickness, crystal perfection or lateral crystal dimension during secondary crystallization, then, an observed increase in the melting temperature must be associated with some changes in the nature or properties of the amorphous phase surrounding polymer crystals.[27,28]

First, we will study the dependence of the melting behavior on crystallization time. We will in particular follow the evolution of the multiple melting endotherms with time and temperature of crystallization. Second, we will follow the evolution of the SAXS profile with crystallization time to verify Strobl's assertion that the lamellar thickness does not change with crystallization time under isothermal conditions. Last, to gauge whether there is in fact increased crystal perfection with longer isothermal crystallization time, we will study the time dependence of the breadth of wide-angle x-ray diffraction (WAXD) peaks for isothermally crystallized samples of it-PS.

CHAPTER 3: EXPERIMENTAL

3.1 Material Used

Keith and Padden observed that the kinetics of crystallization and the morphology of stereoregular polymers are markedly affected by their stereo regularity and purity.[1] Hence, for crystallization studies it is important that such polymer characteristics be controlled and measured accurately. The polymer used in this work is a high tacticty and low polydispersity isotactic polystyrene (it-PS) that was previously purified by H.D. Iler. This material exhibits number and weight average molecular masses, M_n = 425,000 g/mol and M_w = 1,030,000 g/mol, respectively. NMR spectroscopic analysis by H.D. Iler shows that this material has an isotactic content of 97±2%. Since the preparation and characterization of this material were performed in October 1996, and the material has been kept in a screw cap vial since, it is important to assess whether it has undergone any degradation in the intervening time. Spherulitic growth rate measurements were performed on this it-PS to determine whether degradation occurred during storage. If degradation has taken place, the spherulitic growth rate would be expected to increase, in comparison to the growth rate of the sample measured shortly after purification. The change in growth rate arises from enhanced mobility of the lower molecular weight chains during isothermal crystallization.

3.2 Sample Preparation

Film preparation for the SAXS, WAXD, and DSC experiments follows. First a mold "sandwich" is assembled, using stainless steel plates and polyimide sheets. In order to minimize the amount of foreign material present in the films, all of the plates and polyimide sheets were cleaned with acetone and water and subsequently dried using

paper towels and covered until the sandwich was prepared. As each component was layered for the sandwich, dust remover was used on the surfaces, to further mitigate any foreign material. The sandwich structure consists of a stainless steel bottom plate 1.5 mm thick, followed by a polyimide sheet, and then a 0.5 mm stainless steel plate with a circular cavity 20 mm in diameter at the center. Approximately, 0.2 g of the it-PS is placed in the mold cavity. The sandwich is topped with another polyimide sheet, and a 6 mm stainless steel plate. In order to obtain a void-free film, the polymer was stacked into a mound at the center of the mold plate to allow for outward flow during compression. Films were pressed at 250°C using a Carver Laboratory Press Model C hot press and then quenched in an ice-water mixture.

Isothermal crystallization of the isotactic polystyrene films was performed in Blue M ovens, Model M0142SA. A two-point temperature calibration was first performed on two thermocouples and a mercury thermometer using a stirred ice-water mixture and boiling water. The measurements were taken five times each, and the differences between the measured and theoretical temperatures were averaged to determine the correction factor for each thermocouple. Following this, the calibrated thermocouples were used to calibrate the oven temperature. In order to minimize the thermal gradient in the sandwich used for the isothermal crystallization, the sandwich mold was placed between brass plates that had equilibrated to the internal temperature of the oven. The oven was set to the desired crystallization temperature, allowed to equilibrate for one hour, and the temperature was recorded using the two calibrated thermocouples and the mercury thermometer. The mean set temperatures, along with their variances is seen in the following table.

Set T (°C)	Mean Temp (°C)	Standard Deviation (°C)
165	167.3	0.6
175	177.4	0.6
200	202.4	0.9
212	214.6	1.0
215	218.6	0.6
219	221.7	0.7

Table 3.1 - Mean oven temperature and standard deviation

The sandwiches were transferred to the ovens and allowed to isothermally crystallize for 10, 40, and 160 hours. These times were selected based on previous secondary crystallization studies. The longer times ensured that the crystallization process had entered the secondary crystallization region, while also drawing insight to linear change in material properties with logarithmic isothermal crystallization time.[22,24,27,28] At the end of the prescribed crystallization time, the sandwich was quenched in ice water. The film was removed from the mold cavity, dried and prepared for further analysis. Note, the 160 hour oven crystallization experiments resulted in significant oxidation of the it-PS films, so they were not utilized for the remainder of the experimental techniques.

3.3 Optical Microscopy

An Olympus BX50 Polarized Optical Microscope equipped with a CCD camera to capture images and a heating/freezing stage, was used to capture the growth of spherulites under isothermal conditions. The temperature scale of the heating/freezing stage was corrected by comparison of the observed and theoretical melting temperatures of indium. This was performed by placing a thin shaving of indium between two glass coverslips (No. 1, 16 mm, Gold Seal®) that have been wiped with a chemwipe. The indium "sandwich" was then transferred to a Linkham THM 600 furnace-type hot stage with a dry nitrogen purge. There was difficulty observing the melt transition of the

indium, due to the indium showing only marginal flow at its melting temperature. To determine the melting point of indium more accurately, we performed a rapid heating of the indium sample up to 3°C before the stated melting temperature, and then ramped the temperature at a much slower rate (ca. 0.2°C/min) to 5°C past the recorded melting temperature. While performing the slow temperature ramp, the indium sandwich was repeatedly oscillated along the x-axis. The top coverslip would move subsequent to the bottom, and as a result noticeably deform the indium once it had melted. The difference in the observed and literature reported melting temperatures was used to define the correction factor for the heating/freezing stage temperature scale. This calibration was repeated seven times, and the observed melting temperature of indium in the heating/freezing stage was consistently 1.1°C below the literature value.

A description of the spherulite growth rate measurement follows. A polymer sandwich was created in the same manner as the metal used for the temperature calibration. The amount of polymer used was enough to create a film approximate 2 mm in diameter and 50-100 μm thick. The sandwich was then transferred to a Linkham THM 600 furnace-type heating/freezing stage with a dry nitrogen purge, and kept at 250°C. The sandwich was lightly pressed for about ten seconds with the blunt side of a spatula in order to spread the polymer between the coverslips. This was subsequently dropped on a steel plate that had been resting on the surface of an ice bath for quenching. The sample sandwich was transferred back onto the hot stage, which was then sealed and purged with dry nitrogen for about 5 minutes. During that time a temperature program was created where the sample was ramped to 270°C, held for one minute at that temperature to remove any previous thermal history, and subsequently cooled to 190°C, held for one

hour, and then brought to the maximum spherulitic growth temperature of 176.1°C. The temperature was held for one hour at 190°C in order to grow spherulites to a suitable size for measurement; approximately 20 μm.[29] The spherulite growth was recorded at twenty-minute intervals for a spherulite far removed from the edges of the film. It is known that the spherulitic growth rate can be affected by an air interface. The Scion Image software was used to measure the radius of the spherulite (in the unit of number of pixels) as a function of time.

3.4 Wide Angle X-Ray Diffraction (WAXD)

3.4.1 Miniflex

WAXD experiments were performed using a Rigaku Miniflex 600. A graphite monochromator attachment was used, along with a NaI scintillation counter detector, heat exchanger, Cu x-ray tube, and the following slit geometries are utilized for beam refinement: 1.25° divergence slit, 1.25° scattering slit, 0.3° receiving slit, 10 mm length limiting slit, and 5° for the incident and receiving Soller slit boxes. The X-ray tube was operated under a voltage of 40 kV and a current of 15 mA. Scans were performed using a 0.02° step size and a scan speed of 0.5°/minute. Correction for peak position and instrumental broadening was performed using polycrystalline silicon (NIST SRM 640D).[30,31] Film samples were mounted on backed sample holders and then adjusted to the focal height by using clay. Although clay does result in various narrow reflections showing up in the patterns, these are readily identifiable and do not cause broadening of the it-PS peaks. It also does not contribute to the background of the patterns. The position of the monochromator in the Miniflex 600 allows for elimination of Compton scattering. Compton scattering occurs when the X-rays inelastically scatter from the electrons in the

sample. This causes the wavelength of the scattered X-rays to differ from the incident wavelength of 1.5402 Å from the copper $K_{\alpha 1}$. WAXD experiments were carried out at room temperature on it-PS films crystallized for the specific times and temperatures outlined previously.

3.4.2 S-MAX 3000

The experiments were repeated, in part, on a Rigaku S-MAX3000 with a MicroMax-007HF high-intensity microfocus rotating anode X-ray generator in transmission mode. No beam attenuator was needed and the voltage and current used were 45 kV and 30 mA, respectively. Angular calibration was performed by using the position of the third-order diffraction ring from silver behanate, and manually calibrating the sample-to-detector distance. The third-order diffraction ring from silver behanate should occur at $q \approx 0.324$ $Å^{-1}$.[32] The calibrated sample-to-detector distance was found to be 92 mm. This distance was used for angular calibration of all WAXD experiments performed on the it-PS in the SMAX.

Regions of the films produced from isothermal crystallization in the Blue M ovens that displayed minimal oxidation were cut out using a razor blade. They were placed between 0.03 mm-thick Kapton™ films and placed in the heating stage used to record the WAXD experiments at the crystallization temperature. Each scan lasted fifteen minutes. Temperature control of the heating stage was performed using a Linkham heating stage controller, model T95-PE. The temperature was calibrated previously by observing indium melting, as described previously. The diffraction pattern of Kapton™ was recorded at the various crystallization temperatures for further subtraction from the it-PS/Kapton™ sandwich patterns. An in-situ experiment was also performed at 167.3°C,

and wide-angle X-ray diffraction data was collected hourly for ten hours and then once more after fifteen hours of isothermal crystallization. The in-situ experiment was conducted by first melt pressing a film of the it-PS, as described earlier. A void-free section was cut using a razor blade that was approximately 2 mm x 2 mm and anchored in the hot stage between two pieces of the 0.03 mm thick Kapton™ films. The sample was brought to 250°C and held at that temperature for one minute to melt the residual nuclei and erase previous thermal history. It was subsequently cooled to the crystallization temperature using the temperature controller. Patterns were collected on a Fujifilm® Model HR-V image plate with a 0.375" diameter aperture and read using a RAXIA-DI manufactured by Rigaku. After each pattern was collected, the image plate was cleared. For reasons addressed later, only the raw patterns were examined using this method.

3.5 Small Angle X-Ray Scattering

SAXS experiments were performed on a Rigaku S-MAX3000 with a MicroMax-007HF high-intensity microfocus rotating anode X-ray generator. No beam attenuator was needed and the voltage and current used were again 45 kV and 30 mA, respectively. Sections were cut out from the films crystallized isothermally in a Blue M oven using a razor blade. Since oxidation had occurred in some of these films, care was taken to cut out sections that displayed minimal oxidation. Samples were prepared in the same manner as for the WAXD experiments. Patterns were recorded at the predetermined crystallization temperatures for 12 minutes, a time selected to reach a minimum of one million counts and allow for an optimal signal-to-noise ratio. An in-situ isothermal crystallization experiment was performed at 167.3°C, with measurements taken after 1, 2,

4, 10, 15, 20, 25, 30, 35, and 40 hours of crystallization. Additionally, angular calibration was performed by recording the scattering from a piece of silver behenate. Absolute intensity correction was performed by comparing the scattering pattern from a piece of glassy carbon run at Argonne National Laboratory with that from the same piece of glassy carbon on the SMAX. The correction factor was determined only at higher scattering vectors, q, with six points chosen and averaged to produce the correction factor. This value was then multiplied by the thickness of the glassy carbon film, to arrive at the absolute intensity correction factor.

Prior to examination of the raw data, the 2-dimensional scattering patterns were reduced to 1-dimensional intensity vs. scattering vector curves using the SAXSgui program. During this data reduction, the scattering intensities are corrected for X-ray transmission. This proportionally scales the data to account for X-rays that were absorbed by the sample. Absorption corrections were carried out by comparing the intensity recorded by the photodiode for the it-PS film to that of a "blank" sample. If the sample pattern was collected at room temperature, an empty position on the flat sample holder was scanned to obtain the photodiode intensity. When performing scans at the crystallization temperature, the "blank" sample consisted of the Kapton^{TM} films at the corresponding crystallization temperature. The "blank" file was then subtracted out from that of the it-PS pattern. Last, in correcting the pattern for absolute intensity, the thickness of each sample is needed to scale the previously determined correction factor. The sample thickness was obtained by averaging of five measurements at different locations on the same sample. The thicknesses and the variances can be found in Appendix A.

3.6 Differential Scanning Calorimetry (DSC)

DSC heating experiments were performed at a rate of 10°C/min using a TA DSC Q2000 operated with a 50 ml/min nitrogen gas purge. Film samples were obtained by melt pressing a film of purified it-PS in the previously described manner. A section with mass approximately 1.6 mg was cut using a razor blade. This film section was placed in a T-Zero pan manufactured by TA Instruments and placed in the instrument with a pan lid placed gently on top. The pan was transferred to the furnace followed by a temperature ramp to 250°C. The pan was held at this temperature for one minute, and the temperature was subsequently decreased so the pan could be removed and crimped. This initial melting was carried out to maximize the thermal contact between the sample and the base of the pan. In doing so, this ensures a reproducible heat transfer to the sample during crystallization or melting experiments. Once the prescribed crystallization time was reached at the associated temperature, heating proceeded from the crystallization temperature to record the melting behavior. A single sample was used for DSC experiments performed for the 167.3°C and 177.4°C at all crystallization times. A different sample was used for crystallization at each of the higher temperatures. This was due to minimal oxidation/degradation being observed in the films isothermally crystallized in the Blue M ovens at the lower temperatures while in an air environment. However, the nitrogen purge in the DSC mitigates this issue. Consistency between the results presented here and these obtained previously by H.D. Iler further supports our claim that the DSC data was in no way affected by degradation processes.

CHAPTER 4: DATA ANALYSIS

4.1 Optical Microscopy

Determination of the spherulite growth rate at a specific crystallization temperature is carried out by first converting the unit for the radius of a growing spherulite from the number of pixels on the digitized image to a known dimension. The unit conversion factor is measured by take the number of pixels between successive markings on the image of a scale obtained in the same optical microscope/camera system with the same lens configuration. In our experimental set-up, the conversion factor was found to be 1450 pixels/mm. The figure below is a plot of the spherulite radius vs. crystallization time under isothermal conditions (T_x = 176.1°C). The digital images were recorded at twenty-minute intervals. The growth rate is calculated as the slope of the regression line of the radius vs. time data.

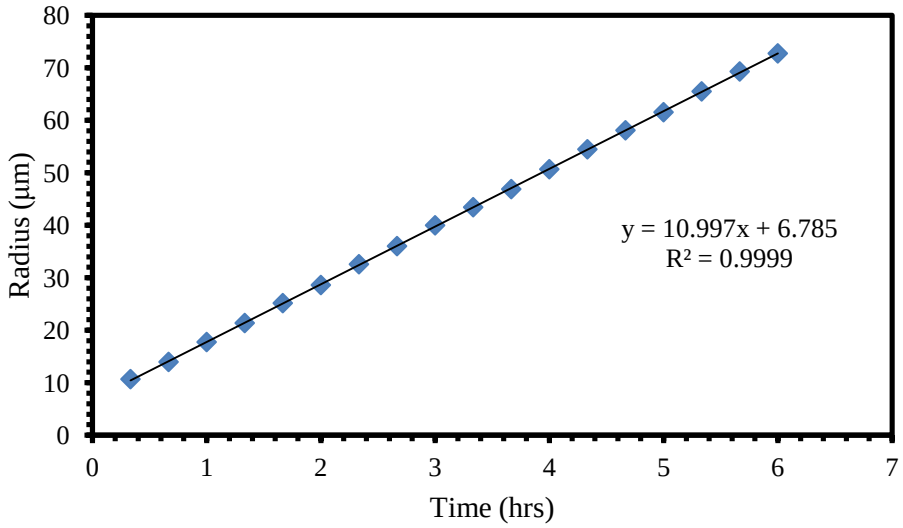

Figure 4.1 - Spherulite radius vs. crystallization time for it-PS at 176.1°C

The it-PS spherulite growth rate measured at 176.1°C was found to be 11.0 μm/hr with a standard deviation of 0.7 μm/hr. This value is essentially identical, within the

experimental uncertainty, to that reported by H.D. Iler in his Ph.D. dissertation ($G = 11.2 \pm 0.44$ μm/hr) for the same material.[29] The variation of spherulite growth rate with temperature measured by H.D. Iler is shown in the following figure.

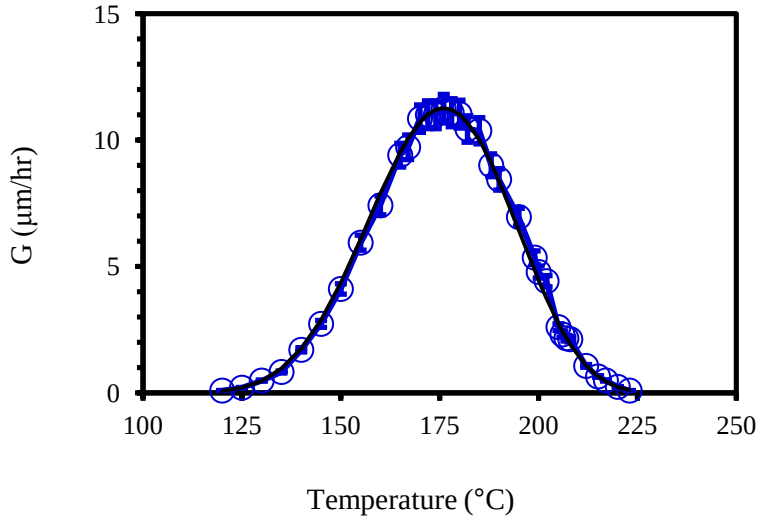

Figure 4.2 - Spherulite growth rate vs. crystallization temperature for it-PS[29]

The observation that the spherulite growth rate measured for this it-PS sample is identical to that measured a number of years ago for the same sample suggests that chemical and photo degradation has been kept to a minimum during storage. Indeed, had either degradation process taken place during storage, the resulting chain scission would have led to a decrease in average molar mass, hence an increase in chain mobility during growth and an increase in spherulite growth rate.

4.2 Wide Angle X-Ray Diffraction

The data from WAXD patterns is given as counts as a function of the diffraction angle (2θ). It is generally necessary to correct the diffraction data for instrumental broadening prior to performing crystallite size and strain analysis. As mentioned previously, polycrystalline silicon (NIST SRM 640D) is generally used angular calibration. However, this standard can also be used to correct for instrumental broadening.[30,31] In experimental

diffraction patterns, the width of diffraction peaks reflects both crystal size and strain but can also be affected by the measurement conditions (instrumental broadening). By taking the diffraction pattern of a large strain-free crystal, which does not result in any diffraction broadening, the broadening of the diffraction peaks can be attributed solely to the instrumental parameters characteristic of the diffractometer. The instrumental broadening can be attributed a multitude of factors, including slit widths, X-ray penetration in the sample, imperfect focusing of the x-rays, and the splitting of the Cu-K_α radiation into two components, $K_{\alpha 1}$ and $K_{\alpha 2}$.[33] Through deconvolution of the instrumental broadening from the measured pattern one is left with the sample pattern, for which the breadth of the diffraction peaks results solely from crystal size and strain.

4.2.1 Instrumental Broadening Correction

To arrive at the pure diffraction profile of the sample, the method of Stokes is described below.[33] Jones[34] was the first to provide the relationship between h(x), the measured diffraction profile, f(y), the sample profile, and g(x-y), the instrumental profile as:

$$h(x) = \int_{-\infty}^{\infty} f(y)g(x-y)dy \tag{4.1}$$

From Shull, Fourier analysis can be used to obtain the sample profile.[35] The terms are redefined in terms of Fourier series as

$$h(x) = \sum H(t)exp\ (-\frac{2\pi ixt}{a}) \tag{4.2}$$

$$f(x) = \sum F(t)exp\ (-\frac{2\pi ixt}{a}) \tag{4.3}$$

$$g(x) = \sum G(t)exp\ (-\frac{2\pi ixt}{a}) \tag{4.4}$$

where t is an integer and H, F, and G are complex coefficients. Values of x are taken in the range of ±a/2 because for each reflection, the diffracted intensity vanishes outside of

that range (only background intensity associated with amorphous and inelastic scattering is left). The complex coefficients are given by

$$H(t) = \frac{1}{a}\int_{-\frac{a}{2}}^{\frac{a}{2}} h(x)\, exp\left(\frac{2\pi i x t}{a}\right) dx \tag{4.5}$$

$$F(t) = \frac{1}{a}\int_{-\frac{a}{2}}^{\frac{a}{2}} f(x)\, exp\left(\frac{2\pi i x t}{a}\right) dx \tag{4.6}$$

$$G(t) = \frac{1}{a}\int_{-\frac{a}{2}}^{\frac{a}{2}} g(x)\, exp\left(\frac{2\pi i x t}{a}\right) dx \tag{4.7}$$

Substitution and simplification into the Jones' relationship yields

$$f(x) = \sum_t \frac{H(t)}{aG(t)} exp\ (-\frac{2\pi i x t}{a}) \tag{4.8}$$

The ratio of the Fourier coefficients is used to pull out f(x), the pure sample profile.[33] A significant assumption is involved with this method, regarding the nature of the standard used to extract the instrumental broadening. The spacing between the diffraction peaks associated with the standard must be large enough that the reflections do not overlap.[37] For the diffraction work reported in this thesis, the instrumental broadening was removed using the PDXL software package purchased from Rigaku USA for the Miniflex 600. The diffraction pattern recorded in the Miniflex 600 for the NIST 640D and the NIST peak listing can be found in appendix B and C.

Smoothing of the line shape and subtraction of the liquid scattering (amorphous background) are necessary steps prior to arriving at the raw data. Smoothing of the line shape is carried out through the use of the B-spline. This method partitions the pattern and fits each segment with a cubic Bézier expression using a least-squares fit.[38] Each resulting expression is connected to replicate the measured pattern. The software background subtraction follows this step, and a fit function is used to remove liquid

scattering. At this point the diffraction pattern is purely a physically broadened profile and can be examined for crystal size and strain. The peaks are identified through comparison with the literature, and the *hh0* family of reflections will be used for crystal size and strain analyses.[39]

4.2.2 Warren-Averbach Method of Fourier Transforms

The Warren and Averbach (WA) method of Fourier transforms stands out as being the analysis involving the fewest a-priori assumptions. Hence, this should be the method of choice for the evaluation of crystal size and strain. [31,33,37,40,41] This method was initially developed to describe stacking faults. However, there are other sources of strain in any crystalline material (i.e. dislocations, point defects, stressed lattice spacing between coherent phases, distorted grain boundaries in nanocrystalline materials, concentration gradients in non-equilibrium multiphase materials, and strains between coherent layered structures, amongst others). [42-48] Highlights of the original method involving an orthorhombic crystal and the *00l* reflection follows, although the method is general enough for any crystal geometry and family of reflections, as seen through a treatment by Warren. [33,49,50]

First, the position of any cell $m_1m_2m_3$, is represented by the vector

$$R_m = m_1a_1 + m_2a_2 + m_3a_3 + \delta m_1m_2m_3 \tag{4.9}$$

where δ is an arbitrary displacement in the crystal that is assumed to be continuous for all unit cells.[51] This assumption allows for a single structure factor, F, to be applied to all cells.[33] The scattering intensity from one crystal is given by

$$I = I_eF^2 \sum_m \Sigma_{m'} exp\,[\frac{2\pi i}{\lambda}(s - s_0) \cdot (R_m - R_{m'})] \tag{4.10}$$

where s_0 and s are the unit vectors of the direction for the primary and diffracted x-ray beam. The quantity of $\frac{s-s_0}{\lambda}$ is the diffraction vector and is given by

$$\frac{s-s_o}{\lambda} = (h_1 b_1 + h_2 b_2 + h_3 b_3) \tag{4.11}$$

where the *b* terms are the reciprocal vectors and the h terms are integers. I_e is the scattering of a single electron. The total diffracted power from the WAXD pattern is given by the powder pattern power theorem, as seen below

$$P = \frac{I_e M j R^2 \lambda^3}{4 v_a} \int\int\int \frac{I_{eu}(h_1 h_2 h_3)}{sin\theta} dh_1 dh_2 dh_3 \tag{4.12}$$

where *M* is the number of crystals in the sample, *R* is the sample-to-detector distance, *j* is the multiplicity, $v_a$is the volume of the unit cell, and $I_{eu}(h_1 h_2 h_3)$ is the intensity per crystal in absolute intensity, as given by 4.10. The total diffracted power can be expressed as a power distribution, with respect to the two-theta angle, and is given by

$$\int P(2\theta) d(2\theta) = \frac{I_e M j R^2 \lambda^3}{4 v_a} \int\int\int \frac{I_{eu}(h_1 h_2 h_3)}{sin\theta} dh_1 dh_2 dh_3 \tag{4.13}$$

In WAXD experiments, the measurement yields the power per unit length of the intersection with Ewald's sphere, as given below

$$P'(2\theta) = \frac{P(2\theta)}{2\pi R sin(2\theta)} \tag{4.14}$$

Expanding and simplifying 4.14 for the *00l* reflection *yields*

$$P'(2\theta) = \frac{P(2\theta)}{2\pi R sin(2\theta)} \sum_{-\infty}^{\infty} N_n(sample) \langle e^{2\pi i l Z_n} \rangle e^{(2\pi i n h_3)} \tag{4.15}$$

The N_n*(sample)* is the number of cells in the sample, Z_n is the displacement vector in the *00l* direction, and *n* is the deviation of the position between the mth cell to the m'th cell in the *00l* direction. The following substitutions are made, where *N* is the number of cells in the sample, *N(col)* is the number of columns in the sample, *N/N(col)* = N_3 the average

number of cells in each column from the *00l* direction, and N_n*(sample)/N(col)* = N_n is the average number of *n* pairs in each column. These allow for 4.15 to be written as

$$P'(2\theta) = \frac{P(2\theta)}{2\pi R sin(2\theta)} \sum_{-\infty}^{\infty} \frac{N_n}{N_3} \langle e^{2\pi i l Z_n} \rangle e^{(2\pi i n h_3)} \quad (4.16)$$

Expansion of the Fourier transforms yields the following

$$P'(2\theta) = \frac{P(2\theta)}{2\pi R sin(2\theta)} \sum_{-\infty}^{\infty} \frac{N_n}{N_3} \{\langle cos(2\pi l Z_n) \rangle cos(2\pi n h_3) - \langle sin(2\pi l Z_n) \rangle sin(2\pi n h_3) +$$

$$i[cos(2\pi l Z_n)\, sin(2\pi n h_3) + sin(2\pi l Z_n)\, cos(2\pi n h_3)]\} \quad (4.17)$$

This is simplified by the fact that each pair of cells along the m_3' and m_3 direction is summed twice, which results in the imaginary contributions being equal but opposite in magnitude and these terms canceling each other out. Further simplification is achieved by introducing the following coefficients

$$A_n = \frac{N_n}{N_3} \langle cos(2\pi l Z_n) \rangle \quad (4.18)$$

$$B_n = -\frac{N_n}{N_3} \langle sin\ (2\pi l Z_n) \rangle \quad (4.19)$$

Substitution into 4.17 yields

$$P'(2\theta) = \frac{P(2\theta)}{2\pi R sin(2\theta)} \sum_{-\infty}^{\infty} [A_n cos\ (2\pi n h_3) + B_n sin\ (2\pi n h_3)] \quad (4.20)$$

Since the sine component is an even function, the B_n coefficients equal zero. Akin to the Stokes deconvolution method, the WA method postulates that the pure diffraction profile of the sample is a convolution of the crystal size and lattice distortion, or strain profile, Fourier coefficients.[37,39,52] This is represented below as

$$A_n = A_n^S A_n^D \quad (4.21)$$

Where the size and strain components are given by

$$A_n^S = \frac{N_n}{N_3} \quad (4.22)$$

$$A_n^D = \langle cos\ (2\pi l Z_n) \rangle \tag{4.23}$$

On the basis of these definitions, the crystal size component is independent of the reflection order, while the strain is not. As the reflection order goes to zero, the strain contribution to the diffraction broadening goes to one. The interval for the intensity versus two-theta region in which the Fourier transform is performed is selected to include the measurable tails of the particular reflection. Specifically, the two-theta angular region for each peak is selected so that the intensity goes to zero on either side of the peak.[33] This is seen in the following figure.

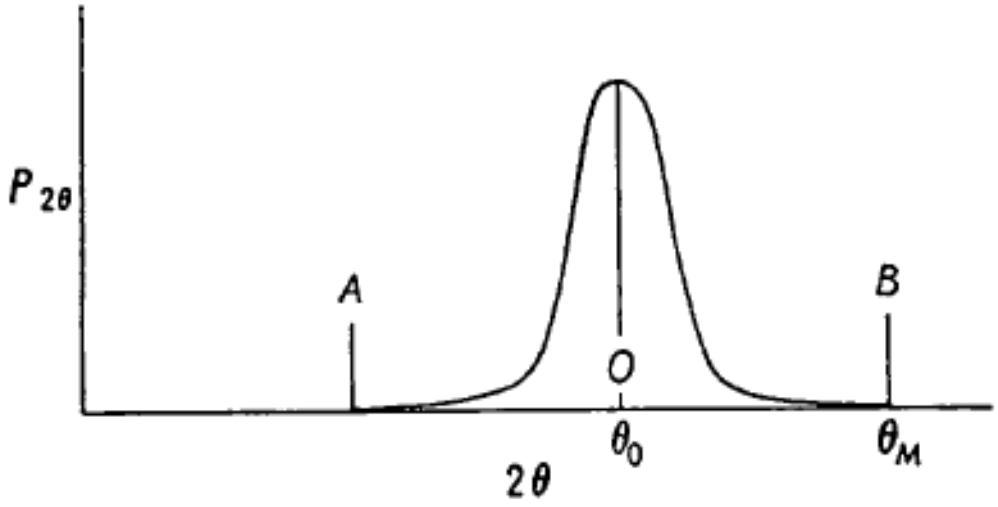

Figure 4.3 - Representative peak interval for Fourier transformation[50]

Since the measurements are performed on a laboratory scale instrument, the coefficients generated are in arbitrary units, rather than in absolute intensity. In order to overcome this, Warren shows that in equation 4.20 when $n = 0$, $N_n = N_3$ and $Z_n = 0$, the resulting cosine coefficient, $A_0 = 1$. The Fourier coefficients from each reflection peak are then normalized to the first Fourier coefficient using this method.[33] In order to separate out the size and strain components, equation 4.21 is rewritten as

$$lnA_n(l) = lnA_n^s + lnA_n^D(l) \tag{4.24}$$

For small values of l and n, the cosine from 4.23 can be expanded to

$$A_n^D = 1 - 2\pi^2 l^2 [\varepsilon_L]^2 \tag{4.25}$$

Substitution of 4.25 into 4.24 and simplifying yields

$$lnA_n(l) = lnA_n^s - 2\pi^2 l^2 \langle {\varepsilon_L}^2 \rangle \tag{4.26}$$

To extract the strain component, which is determined individually as a function of each reflection order, the natural logarithm of the normalized Fourier coefficients for a particular reflection order are plotted vs. l^2, where l^2 is the square of the reflection order. With each successive Fourier coefficient, a linear fit is made between the corresponding "*n"* coefficients from the higher order reflection. Each coefficient corresponds to a higher order harmonic number, where n is given by[53]

$$n = \sum_{k=1}^{n} \frac{1}{k} \tag{4.27}$$

This is demonstrated in a general plot from Warren.

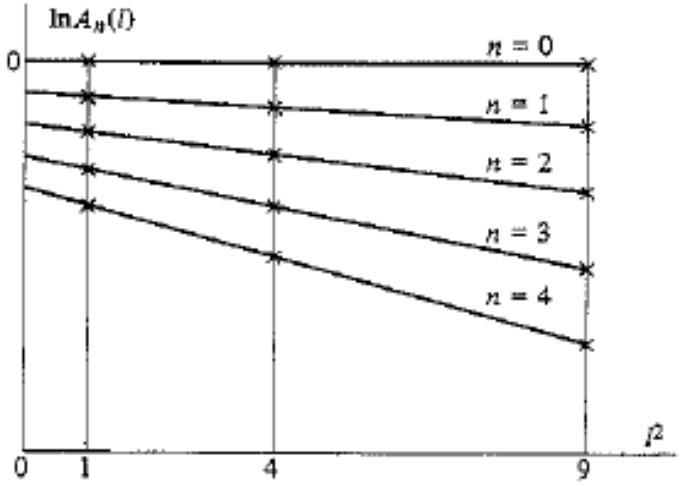

Figure 4.4 - Generic ln(A_n) vs. l^2 plot with linear fitting[33]

The initial slope of the line is equal to $-2\pi^2\langle Z_n \rangle$, and the strain associated with the particular reflection order can be calculated by solving for $\langle Z_n \rangle$. The intercept with the y-

axis for each corresponding linear fit is used to pull out the size contribution to the Fourier coefficient. The exponential is taken of each intercept and then plotted versus the real column length, *L*, in the direction perpendicular to the reflection. The initial slope of the line can then be used to calculate the number average crystal size, <*D*>. Through a mathematical treatment by Bertaut, the intersection of the initial slope of this curve with the x-axis gives the average number of cells per column perpendicular to the reflection plane.[33] This is demonstrated in the following figure.

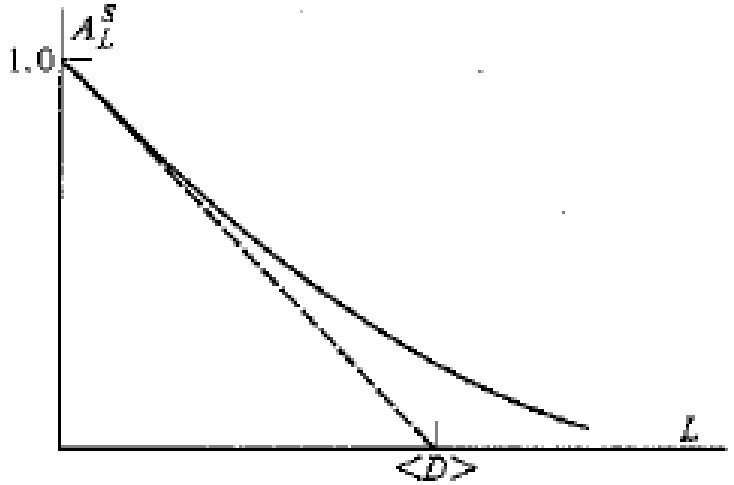

Figure 4.5 - Plot of size component vs. column length, L[33]

The column length, *L*, is different for each reflection order and harmonic number, n_n, and is given by

$$L_n = n_n a_n \tag{4.28}$$

Where a_n is the direction along a particular axis. It is given by

$$a_n = \frac{\lambda}{4}(sin\theta_M - sin\theta_0) \tag{4.29}$$

The angles, θ_M and θ_0, are given by Figure 4.3. Bertaut also shows that by taking the second derivative of the curve, it must be concave upwards.[33] This is evident by the dashed line in the previous figure. If the data results in a "hook" at low *n*, this is evidence

that the subtraction of liquid scattering was underestimated. However, this can be overcome by the normalization of the Fourier coefficients, as mentioned previously. Last, Warren observes that in order to accurately determine the linear extrapolation, a minimum of three orders of a family of planes is required.[49]

4.2.3 Debye-Scherrer Equation

The Debye-Scherrer equation is also used in this study. Although it is a much more general relationship between peak breadth and crystal size, it can be used to provide general insight to crystal size. The equation assumes there is no broadening of the WAXD peaks due to crystal strain, but rather the broadening is due to crystal size. The equation is given below

$$D_{hkl} = \frac{K\lambda}{\beta_0 cos\theta} \tag{4.30}$$

D_{hkl} is the dimension of the crystal perpendicular to the reflection plane, K is a constant that will be taken to be 0.94 for this work, λ is the wavelength of the monochromated X-rays, β_0 is the full-width at half-maximum of the reflection peak in radians, and 2θ is the diffraction angle, in radians. An analysis using the Debye-Scherrer equation will be used to observe whether there are any trends in the crystal size with isothermal crystallization time.

4.3 Small Angle X-Ray Scattering

The ideal two-phase model will be used to extract morphological data from the SAXS intensity profile recorded for the materials studied in this work. The fundamental assumptions for this model are that there are only two distinct phases, each having a unique scattering length density ($\rho_1 \neq \rho_2$) and that their phase boundaries are infinitely thin. We will assume the material is isotropic and has no long-range order. For such a

material, one can define a term Q, known as the scattering invariant, which is related to the integral of the scattering intensity over all scattering angles.

$$Q = \int_0^\infty I(s)s^2 ds \tag{4.31}$$

The scattering invariant is related to the relative amounts of the two different phases when the scattered intensity is given in absolute units. For a two-phase system with sharp phase boundaries, the invariant is given by

$$Q = V(\eta_1^2\phi_1 + \eta_2^2\phi_2) = V(\Delta\rho)^2\phi_1\phi_2 \tag{4.32}$$

Where *V* is the volume, $\Delta\rho = \rho_1 - \rho_2$, is the difference in scattering length or electron density between the two phases, ϕ_n is the volume fraction of phase *n*, and η_n is the scattering length difference between phase *n* and the average, or bulk material.

The figure below shows a representation of the ideal two-phase model, while defining the terms from equation 4.32.

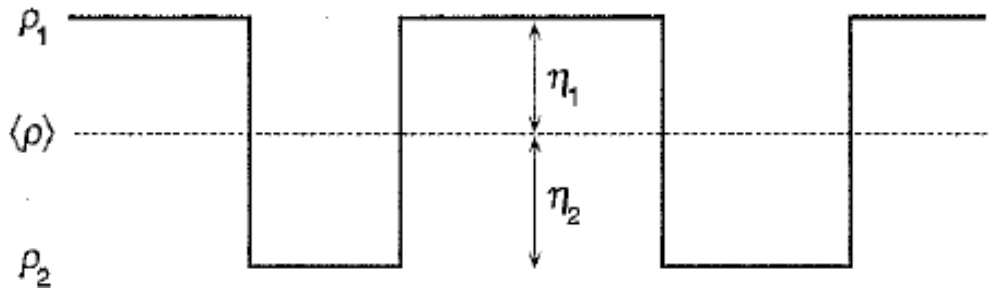

Figure 4.6 - Scattering length density profile for the ideal two-phase model[53]

A fundamental result of the general scattering theory applied to the ideal two-phase model is that, at sufficiently large scattering angle, the scattering intensity obeys Porod's law. This states that the scattering intensity, I(s), decreases as the fourth power of the scattering vector, s^{-4}.[54]

$$\text{For } s \to \infty \quad I(s) \to \frac{2\pi(\Delta\rho)S}{s^4} \tag{4.33}$$

Where S is the total area of the boundary between the two phases. For simplification, the numerator is relabeled K_p, for Porod's constant. An assumption made in deriving Porod's law is that the two phases have homogeneous electron densities, i.e. there are no fluctuations in electron density within the crystalline and amorphous regions. In practice, while it is assumed that the crystal phase is relatively homogeneous, the same assumption cannot be made about the amorphous phase. Indeed, it is well known from wide-angle X-ray diffraction studies that electron density fluctuations exist in the amorphous phase. The amorphous halo is a direct consequence of these fluctuations. The amorphous halo extends to the low-scattering angle region and the scattering present at zero-scattering angle is non-zero as it is a measure of the material's compressibility coefficient. Removal of the amorphous halo, or background correction, must therefore be performed on the data. The scattering data must also be corrected for the fact that the boundaries between the amorphous and crystal phases are actually diffuse. Therefore, before we can make use of Porod's law to analyze the scattering data, corrections must be made on the scattering data for both the diffuse nature of the interfaces (negative deviation from Porod's law) and for the liquid scattering (positive deviation from Porod's law).

The scattering data must also be corrected at low scattering angle to remove the artifacts associated with the presence of a beam stop in the transmission direction during the scattering experiment. The use of a beam stop is required to prevent the powerful incident X-ray beam from hitting the two-dimensional photon detector used to record the weak scattering pattern. If the flux of X-rays striking the detector surface is too large, the detector will be "flooded" with signal and can be damaged. As a result, a beam stop is centered on the detector, where the pinhole collimated x-rays transmitting through the

sample would strike the detector in the greatest population. However, X-rays can be scattered by the beam stop, as seen from the first maximum observed in the scattering profile shown in the figure below.

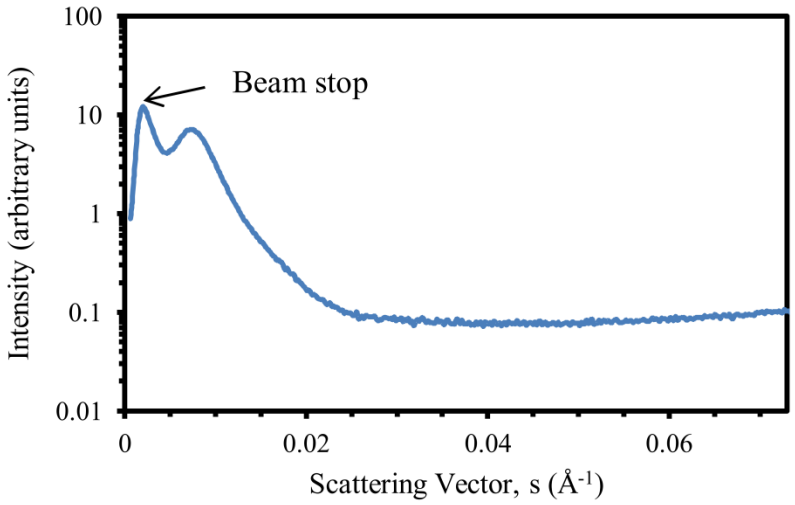

Figure 4.7 - Raw SAXS pattern with artificial beam-stop scattering

The beam-stop scattering is removed through the use of a linear fit to zero-scattering vector from the first local minimum in the scattering intensity. However it is noted that such a method yields a zero-scattering intensity at zero scattering angle, in contrast with expectation that the intensity at zero scattering angle is a function of the thermal density fluctuations within the material and should not vanish.[55] It is therefore preferable to account for the liquid scattering first (background subtraction) and subsequently correct for the beam stop artifacts. Liquid scattering corrections can be achieved following the method outlined by Kortleve, Tuiynman, and Vonk (KTV).[55] In the KTV approach, the scattering data at high scattering angle (~ 0.5 < s < ~ 0.75 $Å^{-1}$, where the low angle tail of the WAXD amorphous halo may be observed) is curve fit using a second-order polynomial of the scattering vector. The polynomial fit takes on the form

$$I(s) = a + b * s^2 \tag{4.34}$$

where *a* and *b* are constants obtained from the fit to the measured intensity. The fit is extrapolated to zero scattering angle using the *a* and *b* values and subtracted from the experimentally observed scattering data to corrected for liquid scattering.[54,55] On subtraction, the scattering intensity at *s = 0* should be positive and close to zero. Note, however, that scattering at low angle reflects heterogeneities over very large distances and does not contribute in a significant manner to the analysis of crystal and amorphous layer thicknesses. Hence, details of the intensity corrections (beam stop and liquid scattering) at low scattering angle are not very important.

The diffuse boundary interface also results in a negative deviation in the value of the scattering invariant, and is due to electron density fluctuations within the amorphous phase. To correct for this deviation a sigmoidal smoothing function is applied to the data

$$I_{corr}(s) = I_{sub}(s)e^{((2\pi\sigma s)^2)} \tag{4.35}$$

Where $I_{sub}(s)$ is the pattern corrected for beam-stop extrapolation and background subtraction. The σ term describes the thickness of the diffuse boundary layer, and is estimated using the treatment from Koberstein et al.[56] for a pinhole collimated X-ray source. This entails plotting $\ln[I(s)s^4]$ versus s^2, for s in the high angle region and then calculating the slope. The slope of the plot is used to calculate σ, given by:

$$\sigma = (\frac{-slope}{4\pi^2})^{1/2} \tag{4.36}$$

This estimation of the diffuse boundary layer thickness differs from the true value by 5% and is simpler than the method outlined by Roe.[57] In the same work, Koberstein et al.[56] present a simplified means to estimate K_p. The intercept is taken from the same region of

$\ln[I(s)s^4]$ versus s^2 used to calculate the diffuse boundary layer thickness. The exponential is then taken of the intercept and this gives the estimated value of K_p. The estimated K_p is then divided by s^4 for the entire range of scattering vectors used in the SAXS experiments. At the point where the estimation for the parameter began in the data, the value of $\frac{K_p}{s^4}$ should be approximately equal to the measured scattering intensity. The measured scattering intensity is then replaced by the Porod extrapolation at the point where the calculation of the parameters begins, and then extended to $s \approx 0.393$ Å^{-1}. Lastly, in order to standardize the high-angle region, the extrapolation for both the diffuse boundary layer thickness and Porod's constant began at twice the scattering vector where the maximum in the scattering intensity occurs and extends through the last positive intensity value.[58] After all these corrections, a scattering curve such as the one shown below is obtained.

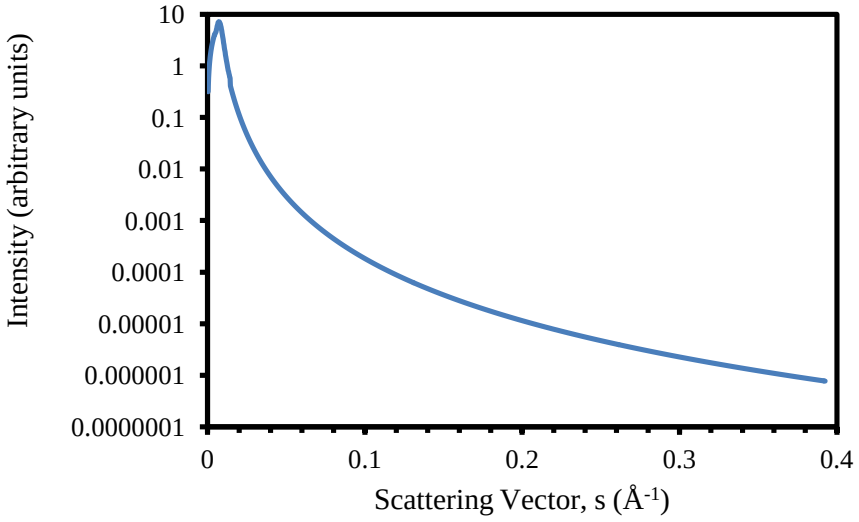

Figure 4.8 - Corrected SAXS pattern for isothermal crystallization at 167.3°C for 10hrs

The SAXS patterns will be analyzed using the 1-Dimensional Correlation Function (1-DCF). From Vonk and Kortleve,[59] performing the Fourier transform of the corrected SAXS intensity curves, yields the electron density autoconvolution. The 1-DCF describes a probability distribution that the same phase exists at two points in the sample separated by some distance, r. The function is given by the following

$$\gamma(r) = \frac{\int_0^\infty I(s)s^2 \cos(2\pi s)ds}{\int_0^\infty I(s)s^2 ds} \tag{4.37}$$

Where the numerator is the Fourier transform of the Lorentz-corrected intensity and the denominator normalizes the data by the scattering invariant.[59] The Lorentz-correction, the s^2 term, is necessary because of the three-dimensional distribution of isotropically ordered lamellae within the sample.[60] A sample 1-DCF curve is seen the following figure.

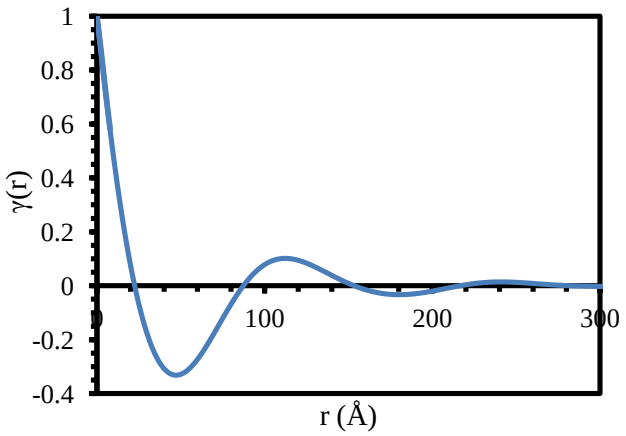

Figure 4.9 - Normalized 1-DCF for it-PS crystallized at 167.3°C for 10hrs

For the 1-DCF method, the dimensions of interest are the lamellar thickness, L_C, long period, L_B, and amorphous layer thickness, L_A. Determination of these parameters follows. The long period is given by the first subsidiary maximum in the 1-DCF curve, and this is then used to calculate L_C, through the following expression

$$L_C = \frac{L_B \pm \sqrt{L_B^2 - 4L_B r_0}}{2} \tag{4.38}$$

where r_0 is determined by taking the slope of the tangent line at the beginning of the curve and then extending the tangent line to the x-axis. The point where this line crosses the x-axis is the value of r_o for equation 4.38.[26] A plot of this can be seen in the figure below.

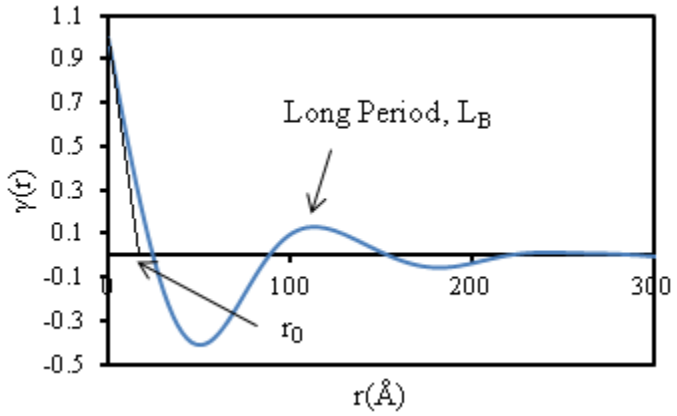

Figure 4.10 - Normalized 1-DCF Showing r_0 and L_B

Note, that when deciding whether to add or subtract the value given by the root, this is determined by coupling the data with DSC experiments. When the crystallinity is less than 50% the root is subtracted from value of L_B, and added when the crystallinity is greater than 50%. Also, the amorphous layer thickness, L_A, is determined by subtracting L_C from L_B. The linear crystallinity is calculated by dividing the crystal thickness by the long period.

4.4 Differential Scanning Calorimetry (DSC)

Data analysis in DSC is fairly straightforward. The TA Universal Analysis software is used to analyze data from the melting events occurring during the heating experiment. The first step involves identifying the melting point from the various melt endotherms, which will be recorded as the melting point of the crystals for the particular

crystallization condition, at that particular heating rate. The melting events are typically broad peaks which are attributed to a number of events that could be occurring during the heating experiment. These events can include lamellar thickening, concurrent crystallization and melting, or simply melting of crystals with a range of dimensions. Therefore for standardization, the peak melting temperature from each melt endotherm is identified during heating experiments for the varying crystallization conditions. This melting temperature can then be used to predict the lamellar thickness by using the modified Gibbs-Thomson equation, which predicts the crystalline dimensions from a thermodynamic basis. The assumption behind the modified Gibbs-Thomson equation is that the polymer crystals have a high aspect ratio, resulting in crystals that are much larger in their lateral dimensions than they are in their thickness and that no thickening of the polymer crystal occurs during melting experiments. Therefore, the thermal stability of the polymer lamellae is limited by its thickness. This is shown in the following derivation.[60] The Gibbs free energy of a crystal is given by

$$\Delta G_{crystal}(T) = 2XY\sigma_e + 2L_C(X+Y)\sigma - XYL_C\Delta G_f^{\infty}(T) \qquad (4.39)$$

where X and Y are the lateral dimensions (i.e. length and width) of a given crystal, σ_e is the fold surface free energy, σ is the lateral surface free energy, and L_C is the crystal thickness. When the crystal is at the melting point, $\Delta G_{crystal}$ in equation 4.39 is equal to zero. From the previous assumptions, the value of XY is much greater than L_C(X+Y), leading to further simplification of equation 4.39 to

$$\Delta G_f^{\infty}(T_m) = \frac{2\sigma_e}{L_C} \qquad (4.40)$$

For a crystal of infinite size at the equilibrium melting temperature, T_m^o, the following is obtained:

$$\Delta G_f^\infty(T_m^o) = \Delta H_f^\infty(T_m^o) - T_m^o \Delta S_f^\infty(T_m^o) = 0 \tag{4.41}$$

And therefore

$$\Delta S_f^\infty(T_m^\infty) = \frac{\Delta H_f^\infty(T_m^\infty)}{T_m^o} \tag{4.42}$$

Below the equilibrium melting temperature

$$\Delta G_f^\infty(T_m) = \Delta H_f^\infty(T_m) - T_m \Delta S_f^\infty(T_m) \neq 0 \tag{4.43}$$

If one further ignores the temperature dependence of the enthalpy and entropy of fusion, then, $\Delta H_f^\infty(T_m) = \Delta H_f^\infty(T_m^o)$ and $\Delta S_f^\infty(T_m) = \Delta S_f^\infty(T_m^o)$. For melting temperatures, T_m, in the vicinity of the equilibrium melting temperature, we obtain

$$\Delta G_f^\infty(T_m) = \Delta H_f^\infty(T_m^o) - T_m \Delta S_f^\infty(T_m^o) \tag{4.44}$$

Substituting in 4.42 into 4.44 yields

$$\Delta G_f^\infty(T_m) = \Delta H_f^\infty(T_m^o)\left[1 - \frac{T_m}{T_m^o}\right] \tag{4.45}$$

And last substituting in 4.40 into 4.45 yields

$$\frac{2\sigma_e}{L_C} = \Delta H_f^\infty(T_m^o)[1 - \frac{T_m}{T_m^o}] \tag{4.46}$$

Which is the Gibbs-Thomson equation. However, this equation is more commonly written as

$$T_m = T_m^o(1 - \frac{2\sigma_e}{\Delta H_f L_c}) \tag{4.47}$$

where T_m is the observed melting temperature, T_m^o is the equilibrium melting temperature and L_c is the crystal thickness. For it-PS, $T_m{}^o$ = 289 ± 5°C, σ_e, the fold surface free

energy is equal to 32.4 mJ/m^2, the enthalpy of fusion is given by ΔH_{fus} = 86.3 J/g and the crystal density is 1.11 g/cm^3.[17,62,63] Rearranging 4.47 to solve for L_c yields

$$L_c = \frac{2\sigma_e}{\Delta H_f(1-\frac{T_m}{T_m^o})} \tag{4.48}$$

Calculating the corresponding crystal thickness from the melting temperature will allow for comparison to thicknesses obtained using SAXS.

The other important piece of information to draw from DSC experiments is the crystallinity present in the polymer sample. This is achieved by integrating the area under the melting endotherms that are present in the trace. As noted previously, there is concurrent crystallization and melting that occurs with the polymer crystals on heating is enabled by the fact that the T_g of it-PS is approximately 100°C and the crystallizations are performed at temperatures above T_g. So despite it-PS crystallizing extremely slowly, there is long-range motion of the polymer chains, and it-PS can undergo a process of melting-recrystallization-remelting. This process may manifest itself in a DSC trace by the presence of one exotherm between endotherms. Therefore in order to standardize the integration to extract the observed enthalpy of fusion, integration began at the onset of melting of the first endotherm and was carried through the last melting event. This is shown in the following figure.

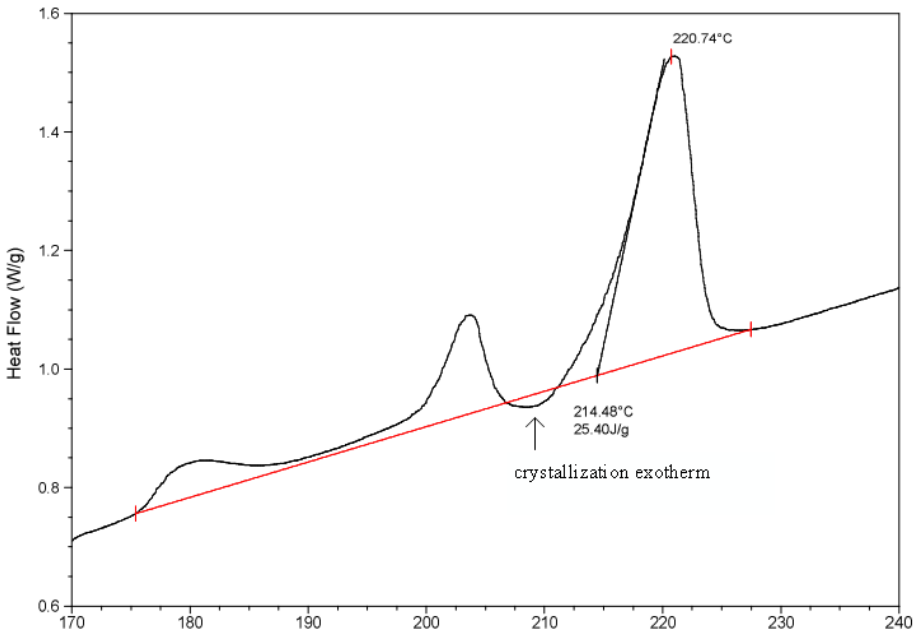

Figure 4.11 – Integrated DSC heating trace after isothermal crystallization at 167.3°C for 10 hrs

The observed enthalpy of fusion can then be used to calculate the degree of crystallinity of the sample. It is arrived by dividing the experimental value by the theoretical value of the enthalpy of fusion for 100% crystalline it-PS. As reported earlier, the Polymer Handbook value for the thermodynamic heat of fusion is $\Delta H_{fus} = 86.3$ J/g.[63] Note that all DSC traces are found in the appendix D.

CHAPTER 5: RESULTS AND DISCUSSION

5.1 Differential Scanning Calorimetry

Typical DSC heating curves (10°C/min) are shown for samples crystallized at 167.3°C, 202.4°C and 214.6°C on Figures 5.1, 5.2 and 5.3, respectively.

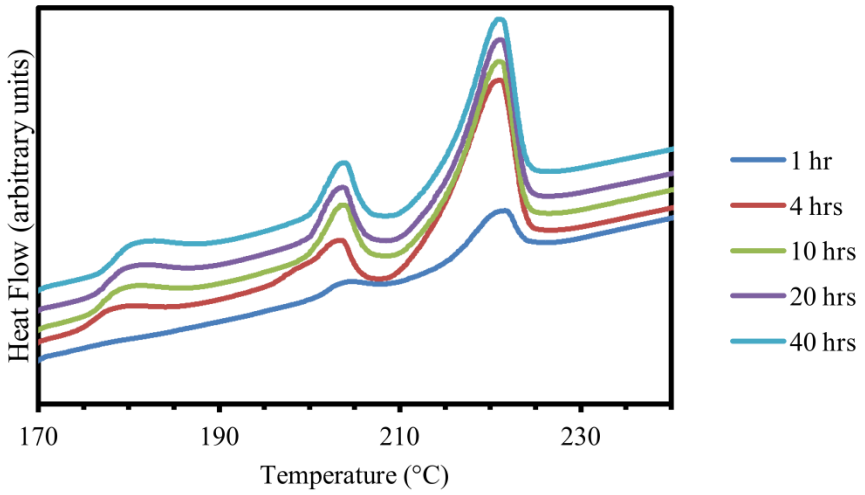

Figure 5.1 DSC heating traces for it-PS crystallized at 167.3°C for different crystallization times

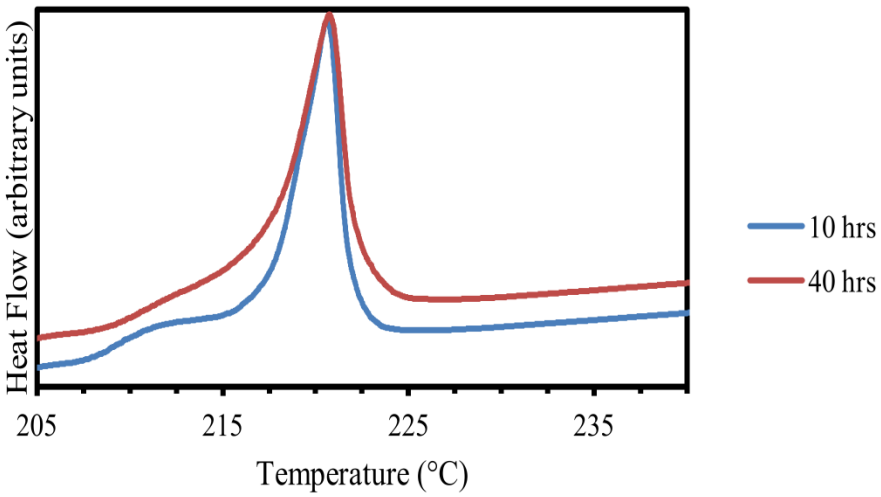

Figure 5.2 DSC heating traces for it-PS crystallized at 202.4°C for different crystallization times

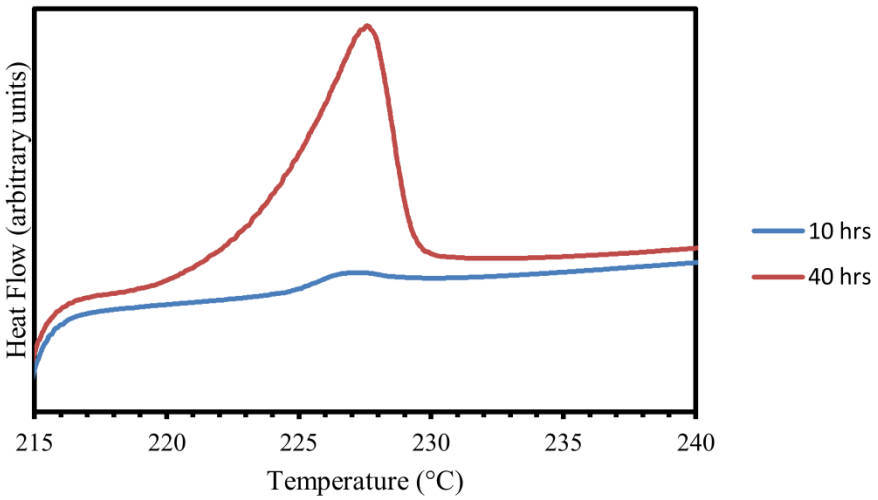

Figure 5.3 DSC heating traces for it-PS crystallized at 214.6°C for different crystallization times

We note a change in the overall melting behavior as crystallization takes place at higher temperatures. For crystallization at 167.3°C (Figure 5.1) three melting endotherms are observed and denoted by I, II and III, in order of increasing temperature. For crystallization at 202.4°C, the intermediate and high endotherms appear to have merged into a single endotherm. Finally, for crystallization at 214.6°C, a single melting endotherm is observed.

The in-situ isothermal crystallization at 167.3°C and subsequent melting experiments yielded the following data for the melting temperatures associated with the lowest, intermediate, and highest endotherms, the overall enthalpy of fusion, ΔH_f, and the degree of crystallinity, X_c, as a function of crystallization time. The degree of crystallinity was calculated using the enthalpy of fusion of 86.3 J/g for a 100% crystalline sample.[61] All melting temperatures are taken as peak temperatures.

Crystallization Time (hr)	T_m(I) (°C)	T_m(II) (°C)	T_m(III) (°C)	ΔH_f (J/g)	X_c
1	176.9	204.2	221.2	3.9	4.5%
2	177.3	203.6	221.2	23.0	26.6%
4	178.7	203.5	221.1	24.8	28.7%
10	179.6	203.7	221.0	25.4	29.4%
15	179.9	203.6	221.0	25.8	30.0%
20	180.1	203.6	221.1	26.1	30.2%
25	180.4	203.7	221.1	26.2	30.4%
30	180.5	203.7	221.1	26.4	30.6%
35	180.7	203.7	221.1	26.6	30.8%
40	181.1	203.7	221.1	26.7	30.9%

Table 5.1 – Transition temperatures, heat of fusion and degree of crystallinity for it-PS crystallized at 167.3°C for different times

As shown on Figure 5.4, the low melting endotherm transition temperature (T_m(I)) varies approximately linearly with the logarithm of crystallization time. This result is consistent with observations made on other polymers.[27,28,64,65]

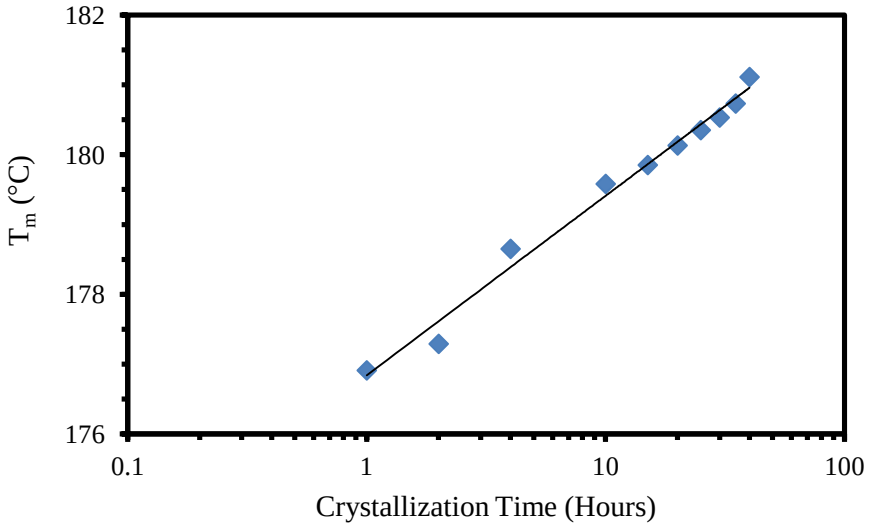

Figure 5.4 – Evolution of the low endotherm transition temperature, T_m(I) vs. crystallization time at 167.3°C

The intermediate, T_m(II), and high, T_m(III), melting temperatures are plotted as a function of crystallization time in Figure 5.5. Figure 5.5 and data in Table 5.1 indicate clearly that

the intermediate and high melting transition temperatures are independent of crystallization time at 167.3°C. The same conclusion can be drawn for samples crystallized at 177.4°C (DSC traces are shown in the appendix D).

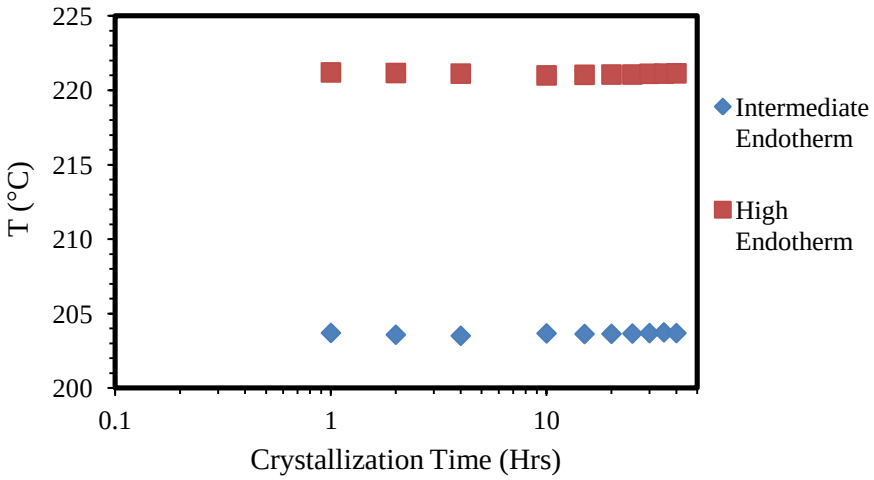

Figure 5.5 – Evolution of the intermediate, T_m(II), and high, T_m(III), endotherm transition temperatures with crystallization time at 167.3°C.

Figures 5.1 to 5.3 show that the crystallization process becomes markedly slower as the crystallization temperature is raised from 167.3°C to 214.6°C. While data was not collected at sufficiently short time intervals during the early stage of isothermal crystallization at 167.3°C, a plot of the DSC degree of crystallinity as a function of crystallization time (Figure 5.6) shows that primary crystallization is complete within the first four hours at 167.3°C, while only a small degree of crystallinity has developed after 10 hrs at 214.6°C (Figure 5.3 and Table 5.2 below).

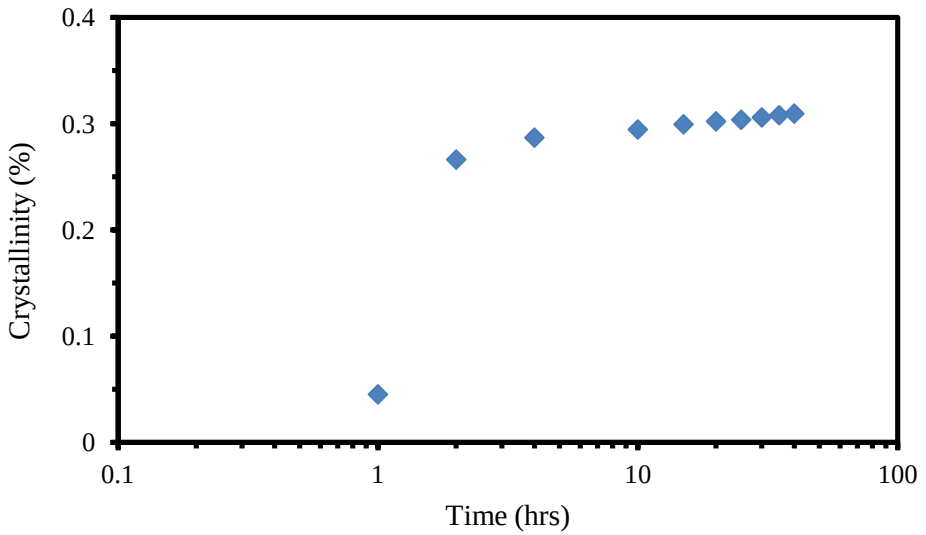

Figure 5.6 – DSC degree of crystallinity as a function of crystallization time at 167.3°C

The following table shows the melting temperatures, enthalpy, and calculated crystallinity for the remainder of the it-PS DSC samples crystallized in-situ at higher temperatures.

Crystallization Conditions	T_m (I) (°C)	T_m (II) (°C)	T_m (III) (°C)	ΔH_f (J/g)	X_c
177.4°C 10 hrs	188.5	207.7	221.6	27.9	32.3%
177.4°C 40 hrs	189.3	207.7	221.6	29.4	34.1%
202.4°C 10 hrs	ND	220.6	NA*	29.8	34.6%
202.4°C 40 hrs	ND	220.7	NA*	32.5	37.7%
214.6°C 10 hrs	NP	227.0	NA*	0.92	1.1%
214.6°C 40 hrs	NP	227.6	NA*	19.8	22.9%
218.6°C 10 hrs	NA**	NA	NA**	NA**	NA**
218.6°C 40 hrs	NP	230.5	NA*	0.86	1.0%
221.7°C 10 hrs	NA**	NA**	NA**	NA**	NA**
221.7°C 40 hrs	NP	232.9	NA*	0.31	0.4%

Table 5.2- Transition temperatures, heat of fusion and degree of crystallinity for it-PS crystallized at different temperatures for different times.

Note that for crystallization at 202.4°C, the low endotherm appears as a shoulder and no peak temperature can be determined (ND). At higher crystallization temperatures

(214.6°C to 221.7°C), the low endotherm was not present (NP) in DSC heating traces, most likely because primary crystallization is still incomplete after 40 hours and secondary crystals only form in measurable fashion after longer crystallization times. Indeed primary crystallinity is not detectable after 10 hrs at 218.6°C or 221.7°C, hence, no data is available for these crystallization times (NA**). The change in crystallization rate with temperature inferred from the DSC data is consistent with the spherulitic growth rate data from Figure 4.2 and confirms that crystallization in this temperature range is indeed nucleation controlled. No information on transition temperatures associated with the upper endotherm is given for crystallization temperatures above 177.4°C as the intermediate and high endotherms have merged into a single peak (NA*).

The peak melting temperatures for the low, intermediate and high endotherms are plotted as a function of crystallization temperature for different times on Figure 5.7.

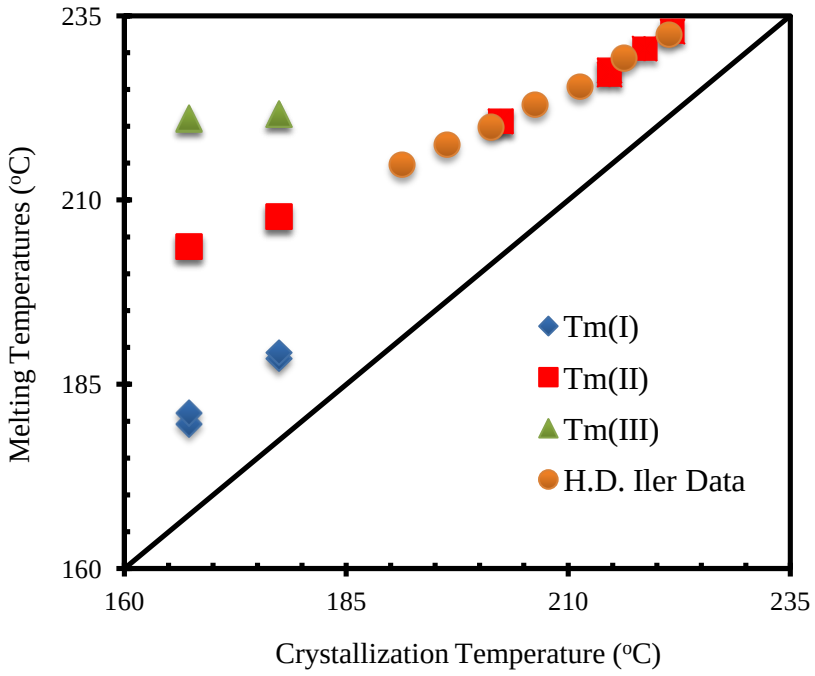

Figure 5.7 - Peak melting temperature as a function of crystallization temperature and time

While very little crystallinity was detected for samples crystallized in the DSC pan at temperatures of 221.7^{o}C for 40 hours, we were initially surprised to note that films isothermally crystallized in the Blue M ovens at this temperature were opaque, which would indicate they are semicrystalline. The disparity between these observations is a direct consequence of the greater ability of it-PS to nucleate on Kapton^{TM} (oven crystallization) than on aluminum (DSC cup) surfaces. In contrast to aluminum, Kapton^{TM} films appear to lower the free energy barrier for primary nucleation, which is especially important for the higher crystallization temperatures.

Using the Gibbs-Thomson equation, it is possible to predict the average lamellar thickness of polymer crystals from their peak melting temperature. This approach was followed for samples isothermally crystallized at temperatures ranging between 167.3^{o}C and 221.7^{o}C. For this calculation, the equilibrium melting temperature was taken as 289^{o}C, the fold surface free energy of 32.4 mJ/m^{2}, the thermodynamic heat of fusion for 100% crystalline it-PS was taken as 86.3 J/g and the crystal density of it-PS was chosen as 1.11 g/cm^{3}.[17,63] The results of such calculations are shown in Tables 5.3 and 5.4 for each melting transition temperature and for samples crystallized under different conditions.

Crystallization Time (hrs)	L_c (Å) from T_m(I)	L_c (Å) from T_m(II)	L_c (Å) from T_m(III)
1	33.9	44.8	56.0
2	34.0	44.5	56.0
4	34.4	44.4	55.9
10	34.7	44.5	55.9
15	34.8	44.5	55.9
20	34.9	44.5	55.9
25	35.0	44.5	55.9
30	35.0	44.5	55.9
35	35.1	44.5	55.9
40	35.2	44.5	55.9

Table 5.3 - Lamellar thickness as a function of crystallization time at 167.3°C predicted by the Gibbs-Thomson equation

Inspection of Table 5.3 suggests that the lamellar thickness increases insignificantly with crystallization time, regardless of which endotherm is associated with the melting of lamellae formed at 164.7^{o}C). The lamellar thicknesses associated with the lowest, intermediate and high endotherms are 35, 45 and 56 Å, respectively. Using the same approach for samples crystallized at higher temperatures leads to the results in Table 5.4.

Crystallization Conditions	L_c (Å) from T_m(I)	L_c (Å) from T_m(II)	L_c (Å) from T_m(III)
177.4°C 10 hrs	37.7	46.7	56.3
177.4°C 40 hrs	38.2	46.7	56.3
202.4°C 10 hrs	ND	55.5	NA*
202.4°C 40 hrs	ND	55.6	NA*
214.6°C 10 hrs	NP	61.2	NA*
214.6°C 40 hrs	NP	61.8	NA*
218.6°C 10 hrs	NA**	NA	NA**
218.6°C 40 hrs	NP	64.9	NA*
221.7°C 10 hrs	NA**	NA**	NA**
221.7°C 40 hrs	NP	67.7	NA*

Table 5.4 - Lamellar thickness as a function of crystallization temperature and time predicted by the Gibbs-Thomson equation

As expected from both the Lauritzen-Hoffman and the Strobl's models, the lamellar thickness increases with crystallization temperature and is independent of crystallization time. We will see in a later section how these lamellar thicknesses compare with actual measurements using small angle X-ray scattering.

We conclude this section by recalling some results published some time ago by Lemstra et al.[66] Lemstra et al. studied the dependence of the melting behavior on heating rate. They showed (see Figure 5.8) that while T_m(III) decreases with increasing heating rate, T_m(I) increases with increasing heating rate. The heating rate dependence of the lowest endotherm is consistent with similar experiments in our laboratory with other polymers.[27,28,64,65]

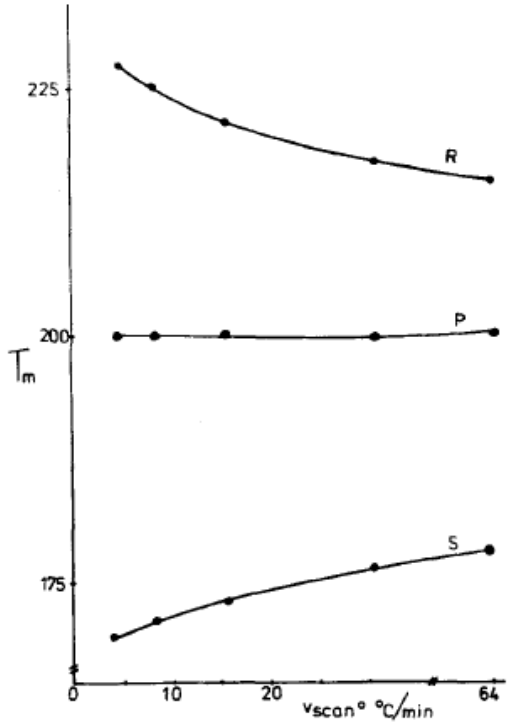

Figure 5.8 – Heating rate dependence on the low, intermediate and high endotherm melting temperatures[66]

This figure also gives insight into the nature of the multiple melting behavior of it-PS. Lemstra et al.[66] argue that the curve labeled P is attributed to the melting of primary crystals, while R is attributed to the melting of polymer lamellae that had recrystallized during the heating scan. Curve S is associated with the melting of secondary crystals. This explanation is fully consistent with later work by Al-Hussein and Strobl[17] but differs from that advanced by Schick et al.[67] Using a "chip" calorimeter they have been able to study the melting behavior of poly(ethylene terephthalate) and it-PS at heating rates up to 30,000 K/min. They suggest that the multiple melting behavior is an artifact associated with melting-recrystallization-remelting in DSC traces of slowly crystallizing polymers under conditions of low heating rates.[67-69] For it-PS, Schick et al.[67] have specifically shown that a single melting endotherm is present in samples crystallized at 140°C and 170°C, when the heating rate is greater than 6,000 K/min. However, studies by Liu and Petermann[70] suggest that Schick's assignment of the lowest melting endotherm to the melting of crystals formed prior to the heating run may be incorrect. Using transmission electron microscopy (TEM), Liu and Petermann compared the lamellar morphology of an it-PS sample crystallized at 160°C for 6 hours to these of samples crystallized in the same condition but subjected to a partial melting process at different temperatures. Partial melting was carried out by holding for a short time an isothermally crystallized sample at a temperature higher than the initial crystallization temperature and subsequent quenching. The various temperatures chosen for the partial melting of it-PS are identified on the following figure. Here, we will only compare the morphologies observed for the as-crystallized sample (arrow a in figure 5.9 and figure 5.10) and the sample partially melted above the lowest endotherm (arrow b and figure 5.11)

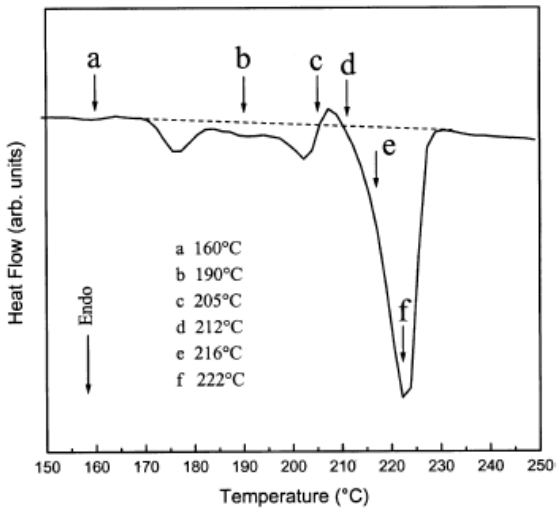

Figure 5.9 - Heating trace of it-PS crystallized at 160°C for 6 hours, identifying the temperatures used for subsequent partial melting before TEM examination[70]

The morphology of it-PS subsequent to isothermal crystallization at 160°C (temperature a) is identical to the morphology of the sample which was subjected to the additional partial melting up to temperature b (see figures 5.10 and 5.11).

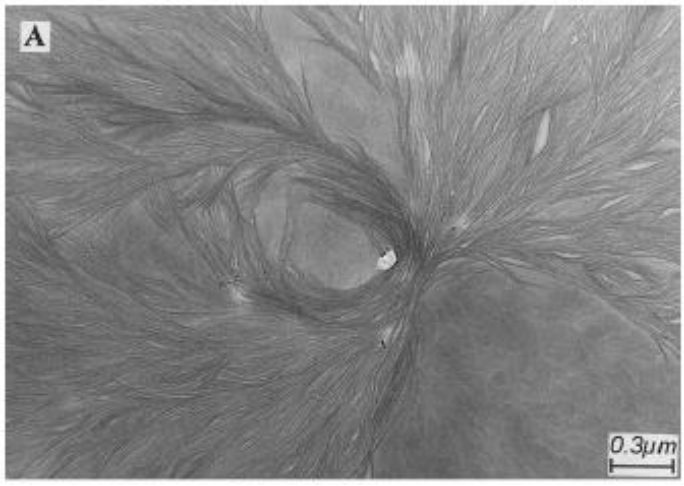

Figure 5.10 – Bright field TEM image of it-PS crystallized at 160°C for 6 hours[70]

Figure 5.11 – Bright field TEM image of it-PS isothermally crystallized at 160°C for 6 hours and subsequently held at T_b for 1 minute[70]

Since the morphology remains the same upon crossing the low temperature endothermic transition, one must conclude that this transition is not associated with the complete melting of the lamellar structures resulting from isothermal crystallization at 160^{o}C.

5.2 Small-Angle X-Ray Scattering

Lamellar thicknesses calculated using the 1-dimensional correlation function analysis for it-PS crystallized in-situ at 167.3°C are given in Table 5.5 and plotted as a function of time in Figure 5.12.

Crystallization Time (hrs)	L_C (Å)	L_B (Å)	L_A (Å)	Linear Crystallinity	σ (Å)
1	32.8	124.8	92.0	26.2%	1.1
2	36.9	119.7	82.7	30.9%	1.9
4	39.7	119.7	80.0	33.2%	2.9
10	35.8	117.1	81.3	30.6%	1.6
15	37.0	117.1	80.2	31.6%	2.0
20	34.5	119.7	85.2	28.8%	1.4
25	37.7	119.7	82.0	31.5%	2.4
30	34.5	117.1	82.7	29.4%	1.5
35	36.2	119.7	83.5	30.2%	2.0
40	38.4	117.1	78.7	32.8%	2.7

Table 5.5-Lamellar thickness of it-PS crystallized in-situ at 167.3°C using the 1-dimensional correlation function analysis

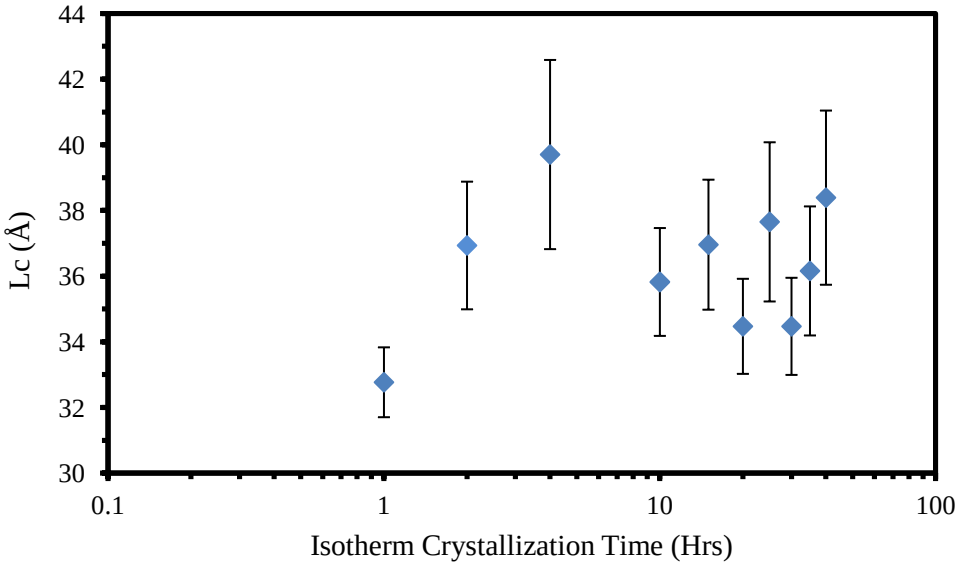

Figure 5.12 – Lamellar thickness (calculated using SAXS data obtained at the crystallization temperature and analyzed with the 1-DCF) vs. crystallization temperature. It-PS was crystallized at different temperatures for 10 hrs and 40 hrs.

The average value of the lamellar thickness for it-PS crystallized at 167.3^{o}C was found to be 36 ± 2 Å. Calculation of the average lamellar thickness ignoring the primary crystallization stage (i.e. before 2 hours of crystallization), yields a value of 37 ± 2 Å.

Therefore, within the experimental uncertainty, the lamellar thickness appears to be independent of crystallization time at 167.3°C. The average long period is 119 ± 2 Å. Just as for the lamellar thickness, all values are independent of crystallization time within the experimental uncertainty.

Lamellar thicknesses were also calculated using the 1-DCF analysis for samples isothermally crystallized in the Blue M ovens and are given in the following table.

Crystallization Conditions	L_C (Å)	L_B (Å)	L_A (Å)	Linear Crystallinity	σ (Å)
167.3°C 10 hrs	30.9	114.4	83.5	27.0%	0.3
167.3°C 40 hrs	31.6	106.8	75.2	29.6%	0.2
177.4°C 10 hrs	31.3	119.4	88.1	26.2%	0.9
177.4°C 40 hrs	33.6	102.1	68.5	32.9%	0.7
202.4°C 10 hrs	43.2	124.6	81.3	34.7%	0.9
202.4°C 40 hrs	44.0	127.1	83.1	34.6%	4.2
214.6°C 10 hrs	49.1	152.6	103.4	32.2%	3.2
214.6°C 40 hrs	51.9	142.4	90.5	36.5%	2.7
218.6°C 10 hrs	63.6	155.1	91.5	41.0%	3.5
218.6°C 40 hrs	63.1	155.1	92.0	40.7%	4.3
221.7°C 10 hrs	62.5	178.1	115.6	35.1%	1.0
221.7°C 40 hrs	65.1	185.6	121.4	34.6%	4.2

Table 5.6-Lamellar thickness calculated from SAXS data recorded at the crystallization temperature and analyzed with the 1-dimensional correlation function. It-PS was crystallized in the Blue M Oven at different temperatures for 10 hrs and 40 hrs.

L_C is plotted as a function of crystallization temperature in Figure 5.13. The lamellar thickness is observed to increase with crystallization temperature, as expected from both the Lauritzen-Hoffman and Strobl models. Within the experimental uncertainty, there is no difference in the magnitude of the lamellar thickness between 10-hour and 40-hour crystallization.

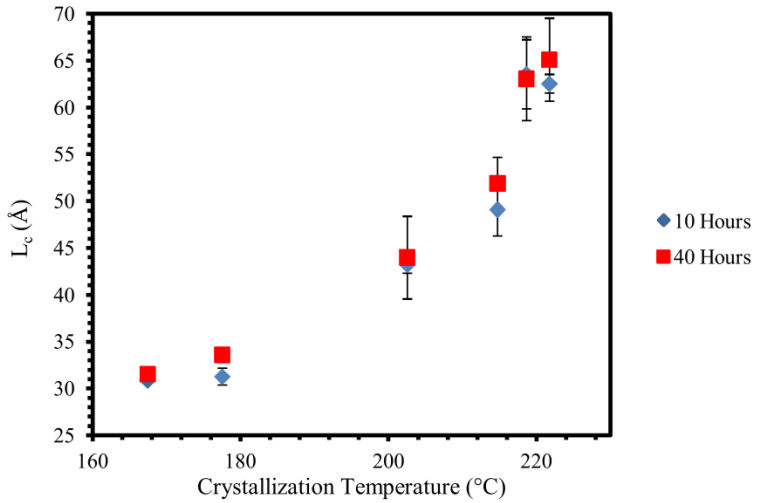

Figure 5.13 - Lamellar thickness (calculated using SAXS data obtained at the crystallization temperature and analyzed with the 1-DCF) vs. crystallization temperature. It-PS was crystallized at different temperatures for 10 hrs and 40 hrs.

Similarly, the long spacing increases with crystallization temperature but does not show any trend with crystallization. In conclusion, both the scattering data recorded in-situ during crystallization at 167.3°C and that recorded at the crystallization temperature after crystallization at temperatures ranging from 167.3°C to 221.7°C, show that the crystal lamellar thickness of it-PS is independent of time during secondary crystallization.

To generate Strobl's melting and crystallization lines require us to identify the melting temperature of lamellae formed at a specific crystallization temperature. We noted in Table 5.2 and Figure 5.7 three endotherms result from isothermal crystallization at 167.3°C and 177.4°C. Depending on the melting endotherm chosen to characterize the melting temperature, the Strobl "nanophase" diagram may look markedly different. In the following three figures, we show this "nanophase" diagram assuming that the melting temperature is associated either with the low endotherm (Figure 5.14), the intermediate endotherm (Figure 5.15) or the upper endotherm (Figure 5.16).

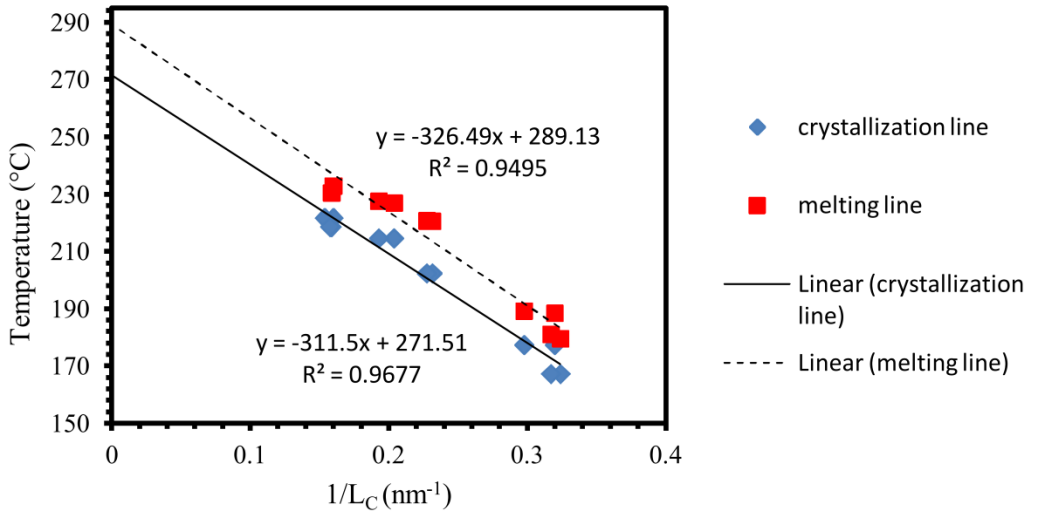

Figure 5.14 – Plot of crystallization and melting lines assuming the melting temperature is given by the low endotherm.

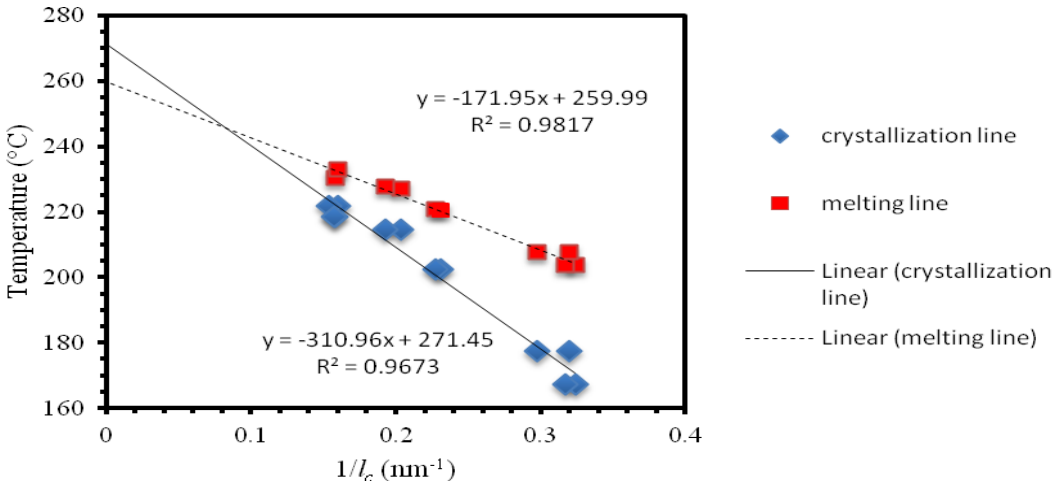

Figure 5.15 – Plot of crystallization and melting lines assuming the melting temperature is given by the intermediate endotherm.

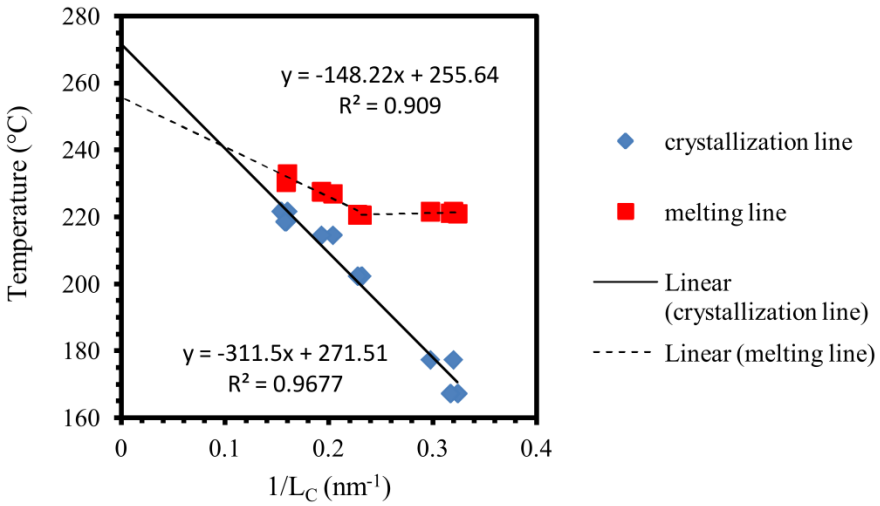

Figure 5.16 - Plot of crystallization and melting lines assuming the melting temperature is given by the high endotherm.

The "nanophase" diagrams represented in Figure 5.14 and 5.16 have significant flaws. First, Figure 5.14 suggests that T_f^{∞} is greater than T_c^{∞}. This is thermodynamically untenable, since it would suggest that the enthalpy changes for the transformations: Crystal → Melt and Mesomorph → Melt are opposite in sign. Second, Figure 5.16 suggests that the melting temperature decreases with increased lamellar thickness for crystallization temperatures between 167.3°C and 202.4°C. Again, this is not expected on the basis of the Gibbs-Thomson equation. Finally, the crystallization and melting lines in Figure 5.15 appear similar to these shown in Strobl's work (see Figure 2.6) with a few important changes, which we will discuss next. Similarities between Figures 5.15 and 2.6 are indeed expected since Strobl claims that the intermediate endotherm indeed corresponds to the melting of lamellae formed under isothermal conditions. However, the equilibrium transition temperatures obtained in this work are very different from these reported by Strobl. The equilibrium melting temperature, obtained by extrapolation of the melting line to the ordinate axis is calculated to be 260°C, while the corresponding value

reported by Strobl is 289°C. Additionally, the equilibrium crystallization temperature obtained in this work is equal to 271°C, while Strobl reports a value of 325°C. Finally, the zero-growth temperature reported by H.D. Iler for the same it-PS material is equal to 260°C. The disparity in the melting lines generated in this work and Strobl's is principally attributed to differences in calculated lamellar thicknesses. Strobl employs Ruland's Interface Distribution Function (IDF) approach[57] for the estimation of lamellar thicknesses, whereas the current work has relied on the 1-dimensional correlation function approach.[17] Strobl associates the distance characteristic of the global maximum in an IDF curve with the lamellar thickness, L_C. This is demonstrated on the following figure, where the points mark the lamellar thickness.

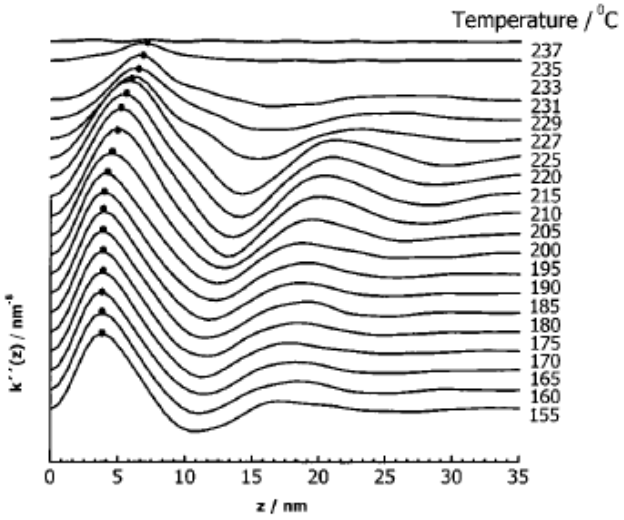

Figure 5.17 – Plot of interface distribution function for it-PS during heating after isothermal crystallization at 155°C[17]

Ruland's IDF approach, however, suggests that there should be two local maxima before the global minimum.[71] Indeed, there has to be one local maximum associated with the most probable crystal lamellar thickness followed by another maximum for the most

probable amorphous layer thickness, followed by one minimum for the long spacing. This is demonstrated in the following figure for a simulated data set by Strobl.

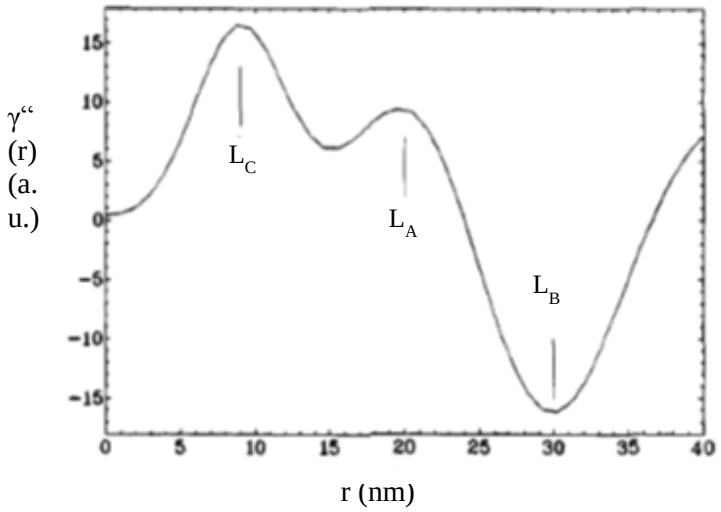

Figure 5.18 – Model IDF curve with lamellar thickness and amorphous layer thickness noted[71]

Experimental data, however, rarely resembles the model curve represented in Figure 5.18 because of overlap of the amorphous and crystal layer thickness distributions. For systems where the crystalline lamellar thickness is smaller than the amorphous layer thickness, an overlap of the two distributions would be expected to lead to higher apparent crystal thickness value obtained by the IDF approach than by the 1-DCF approach. Evidence supporting this assertion is given in Table 5.7. The lamellar thicknesses calculated from the 1-DCF in this work are lower than the expected lamellar thicknesses obtained by Strobl from his crystallization line data, using Ruland's IDF approach. This is especially prevalent at the lowest temperatures of crystallization when the linear degree of crystallinity is much below 50%. Note, however that the difference between the results obtained by these two methods decreases when the linear crystallinity (L_c/L_B) approaches 50%. This is evident from Table 5.7 where the linear crystallinity

increases with higher crystallization temperature, reaching a maximum at T_x = 218.6°C (~41%) using the 1-DCF analysis method. At this temperature, the difference in calculated lamellar thickness between the IDF and 1-DCF methods is the least. However, the linear crystallinity at T_x = 221.7°C is less than T_x = 218.6°C, causing the difference in calculated thicknesses to increase again.

T_x (°C)	L_c^{IDF} (Å)	$L_c^{1\text{-}DCF}$ (Å)
167.3	43.2	31.2
177.4	46.1	32.4
202.4	55.6	43.6
214.6	61.7	50.5
218.6	63.9	63.3
221.7	65.9	63.8

Table 5.7 – Comparison of lamellar thickness data as a function of crystallization temperature: L_c^{IDF} was calculated Strobl et al.[17] using the IDF; $L_c^{1\text{-}DCF}$ was calculated here using the 1-dimensional correlation function approach.

Regarding the melting line, one should note that different heating rates were used in the DSC experiments in Strobl's work and in this work. However, Lemstra et al.[66] showed (see Figure 5.8) that while the respective locations of the low and high melting endotherms are affected by the heating rate used, the intermediate endotherm is independent of heating rate (in the range from 4 to 64 K/min). Hence, our intermediate endotherm melting temperatures are comparable to those reported by Strobl.

Let us summarize our results obtained on the basis of small angle X-ray scattering. The present data rules out crystal insertion as a mechanism for secondary crystallization. Indeed, if crystal insertion between primary crystals had occurred during secondary crystallization, one would expect that both the long period and the lamellar thickness should decrease with increase in crystallization time, as claimed by Hsiao et al.[20] and Wang et al.[71] The data shown here also rules out lamellar thickening as the

secondary crystallization mechanism for it-PS. Indeed, if thickening were to occur in the primary lamellae, the lamellar thickness would increase at the expense of the long period. Our results confirmed the work done by Lemstra et al.[66] where they found no evidence of lamellar thickening in it-PS during secondary crystallization. The crystallization and melting lines derived on the basis of calorimetric and scattering data are qualitatively similar to these reported by Strobl. However, the calculated equilibrium melting temperature and equilibrium crystallization temperature are, within experimental error, identical to the zero growth temperature reported by H.D. Iler in his Ph.D. dissertation.[29] This last result casts some very serious doubt as to the validity of the Strobl model of polymer crystallization. In the next section, we will address another facet of Strobl's model, i.e. the evolution of lateral crystal dimensions during crystallization.

5.3 Wide-Angle X-Ray Diffraction

Admittedly, the diffraction peak broadening data was analyzed in reverse order, where a more complicated treatment (Warren-Averbach method) was initially applied unsuccessfully to the data, prior to using the Debye-Scherrer method. The data generated through the Warren-Averbach (WA) and the Debye-Scherrer analyses are given below. The first table (Table 5.7) gives crystal size (D_{hh0}) and crystal strain for the (110), (220) and (330) reflections as a function of time for a sample crystallized at 167.3°C. The diffraction data was obtained at room temperature subsequent to crystallization. The WA method resulted in crystal dimensions that were much lower than expected and neither the crystal size nor the strain showed any trend as a function of crystallization time.

Crystallization Time (hrs)	D_{hh0} (Å)	Reflection Order Strain		
		110	220	330
1	45.5	4.2%	2.2%	2.2%
2	43.5	3.8%	3.1%	2.3%
4	48.1	8.4%	5.6%	8.6%
10	41.3	1.7%	1.0%	NO
15	53.5	1.5%	NO	NO
20	40.3	1.1%	3.0%	4.2%
25	39.2	0.1%	0.1%	1.1%
30	81.3	2.7%	NO	NO
35	43.7	0.5%	6.4%	6.1%
40	89.3	2.6%	6.2%	3.2%

Table 5.8 – WA analysis for it-PS crystallized at 167.3°C for different times. Diffraction data recorded at room temperature.

Sample	D_{hh0} (Å)	Reflection Order Strain		
		110	220	330
177.4°C 10hrs	52.9	0.8%	5.6%	2.1%
177.4°C 40hrs	66.7	1.4%	2.5%	NO
202.4°C 10hrs	47.6	0.4%	2.2%	1.9%
202.4°C 40hrs	277.8	3.8%	4.0%	3.7%
214.6°C 10hrs	35.0	0.5%	3.6%	1.2%
214.6°C 40hrs	40.0	3.9%	1.9%	2.2%
218.6°C 10hrs	46.9	0.2%	NO	NO
218.6°C 40hrs	87.7	1.1%	NO	NO
221.7°C 10hrs	54.6	0.6%	1.1%	2.4%
221.7°C 40hrs	38.2	0.4%	0.3%	0.2%

Table 5.9 – WA analysis for it-PS crystallized at different temperatures for 10 hrs and 40 hrs. Diffraction data recorded at room temperature.

Again the crystal dimensions are too low to be credible and neither the strain nor the crystal sizes show any trend as a function of temperature of crystallization. Therefore, the data generated from the WA method are not considered in the remainder of this work. We believe that our application of the WA method to our data was flawed as a result of the PDXL software incorrectly subtracting the amorphous halo. Specifically, we believe we underestimated the contribution from the tails of diffraction peaks and overestimated the

scattering from the amorphous halo in the vicinity of the diffraction peaks. Since the application of the WA method to our diffraction data was not successful, we resorted to the use of the Debye-Scherrer equation to extract apparent crystal lateral dimensions from the breadth of appropriate lattice reflections. The following table gives the apparent crystal sizes obtained by the Debye-Scherrer analysis for the 110 and 220 reflections of diffraction patterns obtained at room temperature subsequent to isothermal crystallization at 167.3°C. The full-width at half maximum (FWHM) values was generated by the PDXL software package from Rigaku.

Crystallization Time (hrs)	**D_{110} (Å)**	**D_{220} (Å)**
1	255.4	196.6
2	253.3	216.8
4	245.7	199.7
10	242.0	196.9
15	229.8	216.7
20	240.9	208.6
25	239.3	213.2
30	204.4	174.4
35	215.4	190.1

Table 5.10 – Debye-Scherrer analysis on it-PS crystallized for different times at 167.3°C. Diffraction pattern was recorded at room temperature.

Values, D_{hh0} , of the apparent crystal size are plotted as a function of crystallization time in Figure 5.19.

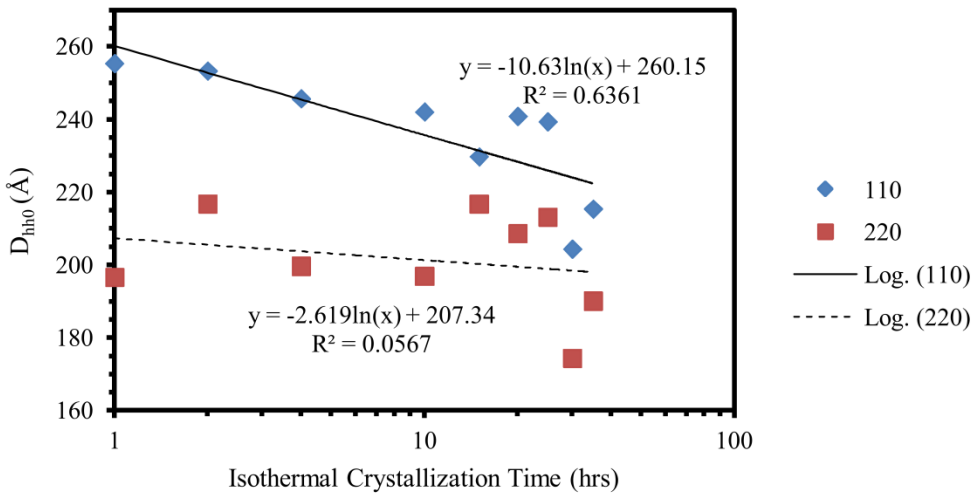

Figure 5.19 – Apparent crystal size calculated (using the Debye-Scherrer equation) vs. crystallization time for it-PS crystallized at 167.3°C. Each diffraction pattern was recorded at room temperature.

The diffraction data associated with it-PS crystallized for 40 hrs was considered to be an outlier and was discarded during the analysis. This was due to that data point predicting the crystal lateral dimension to be significantly below the observed trend. The analysis did not require subtraction of the amorphous halo from the diffraction pattern of the semicrystalline material since it does not affect the full-width at half maximum of the reflection. Although the data does show significant scatter, one may be tempted to conclude that with longer isothermal crystallization time, a decrease is observed in the apparent crystal size. The scatter in the data is believed to be associated with improper mounting of the it-PS sample in the diffractometer. Indeed, it is known that even a slight tilt in the sample orientation in the diffractometer or uneven film surface can lead to changes in the breadth of the reflection. To avoid having to mount and dismount it-PS samples in the diffractometer, so as to collect diffraction patterns for samples crystallized for different times, we recorded diffraction patters in-situ during crystallization of it-PS

in a hot stage in the S-MAX 3000 camera. The full-width at half-maximum was estimated manually from the diffraction patterns and analyzed with the Debye-Scherrer equation. Again, only raw patterns were used, since removal of liquid scattering would not affect the FWHM and peak position.

Crystallization time (hrs)	FWHM (rad)	Peak (rad)	D_{110} (Å)
1	0.006351	0.0700	228.5
2	0.006457	0.0703	224.8
3	0.006366	0.0700	228.0
5	0.006558	0.0700	221.3
6	0.006994	0.0703	207.5
7	0.006831	0.0700	212.5
8	0.007084	0.0700	204.9
9	0.007411	0.0700	195.8
10	0.006732	0.0700	215.6
15	0.007686	0.0703	188.8

Table 5.11 –Debye-Scherrer analysis of the 110 reflection as a function of crystallization time at 167.3°C. Diffraction patterns were recorded at the crystallization temperature.

Crystallization time (hrs)	FWHM (rad)	Peak (rad)	D_{220} (Å)
1	0.006921	0.1396	211.2
2	0.007122	0.1401	205.3
3	0.007031	0.1396	207.9
5	0.007012	0.1399	208.5
6	0.007378	0.1401	198.1
7	0.007266	0.1399	201.2
8	0.008147	0.1396	179.5
9	0.008208	0.1401	178.1
10	0.008322	0.1401	175.7
15	0.008455	0.1401	172.9

Table 5.12 – Debye-Scherrer analysis of the 220 reflection as a function of crystallization time at 167.3°C. Diffraction patterns were recorded at the crystallization temperature.

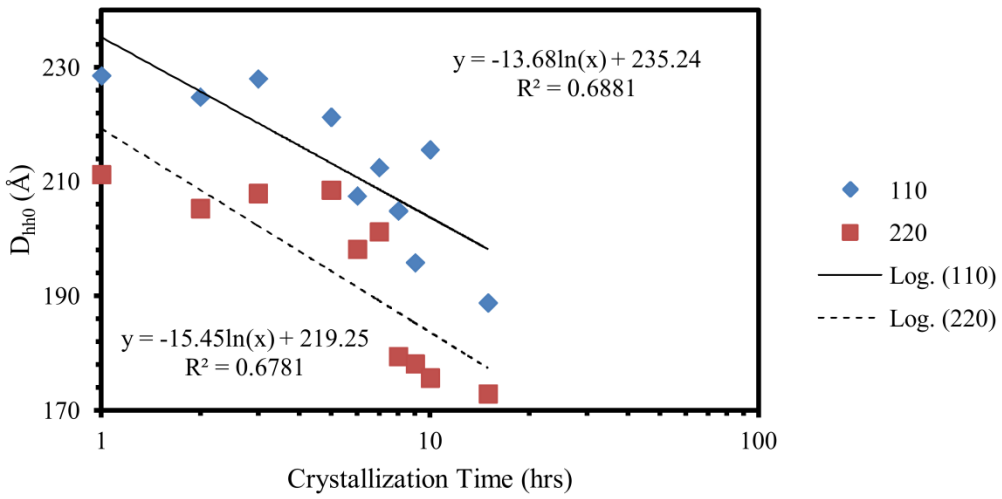

Figure 5.20 – D_{hh0} vs. isothermal crystallization time at 167.3°C

Figure 5.20 clearly demonstrates that the number average crystal size decreases with increased crystallization time. The first important conclusion drawn from this data is that secondary crystallization and structural stabilization are not associated with a decrease in crystal strain or an increase in crystal lateral dimensions. These changes in the properties of lamellar crystals would have given rise to a decrease in diffraction peak breadth with increase in crystallization time. We recall that Alfonso et al.[24] had explained PET's crystal stabilization during secondary crystallization (inferred from the shift of the low endotherm to higher temperatures during the secondary crystallization) in terms of an increase in crystal lateral dimensions. We can conclude now that while the observation of a shift in melting endotherms to higher temperature with increasing crystallization time is a nearly universal phenomenon, the concurrent increase in crystal lateral dimensions is not universal. Therefore, it cannot be used to explain the crystallization time dependence of the melting behavior. Since an increase in either crystal lamellar thickness, crystal perfection or crystal lateral dimensions is not observed during the secondary crystallization of it-PS, a mechanism involving the amorphous fraction of semicrystalline

polymers may need to be invoked. First, we should note that a decrease in the average lateral crystal dimensions of it-PS with time is consistent with an increase in the population of smaller, less perfect crystals during secondary crystallization. Small secondary crystals can be viewed, according to Marand et al.,[27] as crosslinking sites in the remaining amorphous fraction. As the fraction of small crystals, i.e. crosslinking sites, increase during secondary crystallization, the glass transition temperature should increase with secondary crystallization time. This behavior has indeed been observed in the case of PET, it-PS and PEEK and is highlighted below in the case of PEEK (Figure 5.21). Note that PEEK's T_g increases linearly with the logarithm of crystallization time, during secondary crystallization, in very similar manner with the peak temperature associated with the low endotherm observed in this work. The WAXD data presented here is the first set of data that demonstrates an increase in the population of small crystals during secondary crystallization, hence, provides a justification for the increase in glass transition temperature with longer crystallization time.

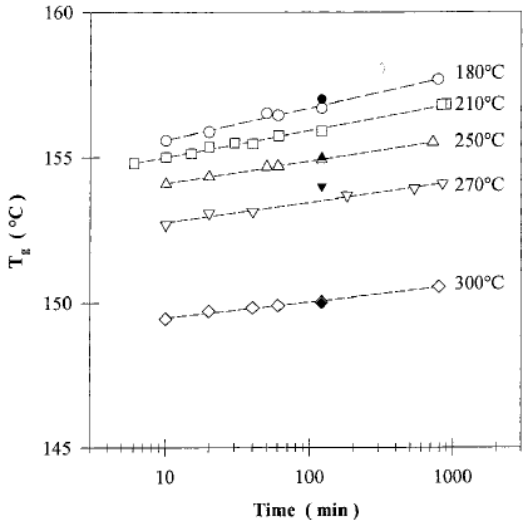

Figure 5.21 – Evolution of T_g for PEEK with varying thermal history during secondary crystallization[27]

An increase in glass transition temperature with secondary crystallization time is consistent with an increase in constraints in the amorphous fractions surrounding polymer crystals and is consistent with a mechanism that retards the melting of such crystals. Indeed an increase in conformational constraints is expected to decrease the entropy of the amorphous fraction, hence, raise the melting temperature. In conclusion, this study suggests that secondary crystallization leads to a reduced mobility of the polymer chains in the remaining amorphous fraction, hence, is at the origin of the time dependent melting behavior. This stands in direct contrast to Strobl's model, which claims that an increase in lateral dimensions (nascent to stable crystal transformation) is at the origin of the time-dependent melting behavior.

CHAPTER 6: SUGGESTED FUTURE WORK

A great deal of work remains to be carried out to study the origin of the time-dependent melting behavior of semicrystalline polymers.

First WAXD peak broadening analyses need to be extended to different crystallization temperatures. The conclusion drawn in this work that conformational constraints may develop in the amorphous phase as a result of secondary crystallization is based on data obtained at a single crystallization temperature. Repeating the isothermal crystallization experiments at lower crystallization temperatures is ideal in part because oxidation/degradation effects will be minimal. The lower crystallization temperatures will also us to access the secondary crystallization at shorter times than at higher temperatures, due to increased nucleation. Ideally, the diffraction experiments should be carried out in-situ during crystallization to minimize artifacts associated with repeated sample unloading and reloading in the diffraction set-up. Experiments could also be performed at higher crystallization temperature if the heating stage can be modified to operate under inert gas purge. The Debye-Scherrer analysis should be supplemented by the more rigorous Warren-Averbach (WA) approach to separate crystal size effects from strain effects. Use of the WA method will necessitate a more accurate subtraction of the amorphous halo. This should be carried out using diffraction patterns obtained at each crystallization temperature before crystallization sets-in. To obtain such amorphous scattering pattern should not be difficult since it-PS crystallization is extremely slow. Since the thermal density fluctuations in the amorphous phase vary with temperature, it is indeed important to carry out the amorphous halo subtraction with that characteristic of the crystallization temperature of interest.

Further exploration of the melting behavior needs to be carried out by fast calorimetry using the Flash DSC, as pioneered by Schick. Two considerations make this technique significantly more insightful than conventional DSC. In conventional DSC heat flows in and out from the base of the pan through a sample of finite thickness. This results in a significant thermal gradient being present in a sample, especially at high heating or cooling rates. As a result, the heat flow signal observed is broadened and delayed and the resolution in melting temperature decreases with increased heating or cooling rates. Unfortunately, sufficiently high heating rates are necessary to inhibit melting-recrystallization-remelting effects. Indeed, Schick et al. showed that the multiple melting behavior disappears and a single melting endotherm is observed during the heating of it-PS at rates higher than 6000 K/min (see Figure 6.1).

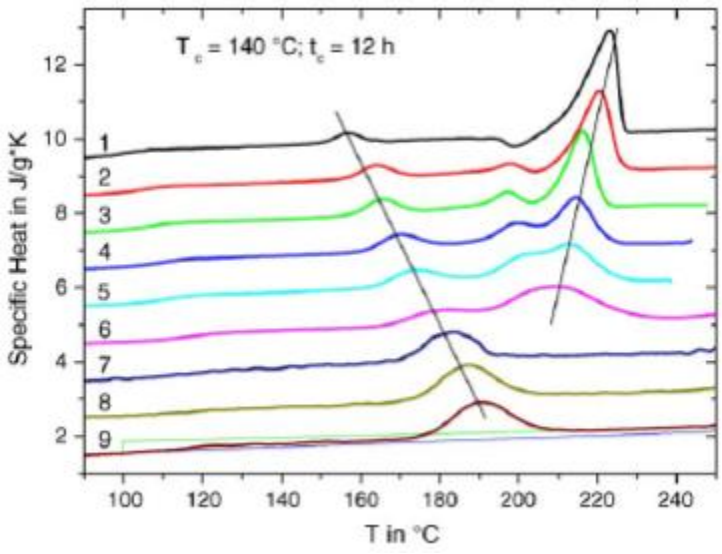

Figure 6.1 - Evolution of the melting behavior of it-PS with heating rate

(1) 10 K/min, (2) 50 K/min, (3) 100 K/min, (4) 200 K/min, (5) 400 K/min, (6) 500 K/min, (7) 6000 K/min, (8) 15,000 K/min and (9) 30,000 K/min[67]

Heating experiments will be carried out after crystallization at different temperatures for different times. It will be interesting to determine whether the melting of lamellae formed under isothermal conditions is associated with the first endotherm as suggested by Schick's work or with the intermediate endotherm as claimed by Strobl. Confirmation of Schick's result will have some significant consequence for the meaning of the nanophase diagram and the associated thermodynamic model of Strobl. The crystallization time dependence of the melting behavior observed at low heating rate needs to be compared to that measured at high heating rate. Specifically, the rate of shift of the low endotherm (low heating rate experiments) will be compared to the rate of shift of the single endotherm (high heating rate experiments) with the rate at which the diffraction broadening takes place under isothermal crystallization. Finally, the crystallization time and temperature dependence of the glass transition temperature should be determined. These latter measurements will provide information on the level of conformational constraints in the amorphous fraction. A similar crystallization temperature dependence for these four rates would provide further support for the idea that secondary crystallization occurs by a process of new crystal formation, where the secondary crystals increase the conformational constraints in the remaining amorphous fraction, hence exhibit higher melting temperature.

BIBLIOGRAPHY

1. Keith, H.D., Padden, F.J., *J. Appl. Phys.*, 35, 4, 1270 (1964)
2. Keller, A., O'Connor, A., *Discuss. Faraday Soc.*, 25, 114 (1958)
3. Keller, A., Sawada, S., *Die Makromol. Chem.*, 74, 190 (1964)
4. Pae, K.D., Morrow, D.R., Sauer, J.A., *Nature*, 211, 514 (1966)
5. Palmer, R.P., Cobbold, A.J., *Die Makromol. Chem.*, 74, 174 (1964)
6. Blundell, D.J., Keller, A., Ward, I.M., *Polym. Lett.*, 4, 781 (1966)
7. Lauritzen, J.I. Jr., Hoffman, J.D., *J. Res. Natl. Bur. Stand., Sect. A*, 64, 73 (1961)
8. Strobl, G., *Eur. Phys. J. E*, 18, 295, (2005)
9. Hoffman, J.D., Miller, R.L., *Polymer*, 38, 17, 3151 (1997)
10. Bassett, D. C. Principles of Polymer Morphology. Cambridge UP, New York, 1981
11. Strobl, G., *Rev. Mod. Phys.*, 81, 3, 1287 (2009)
12. Hoffman, J. D.; Miller, R. L.; Marand, H.; Roitman, D. B. *Macromolecules*, *25*, 2221 (1992)
13. Strobl, G., *Prog. Polym. Sci*., 31, 398 (2006)
14. Keller, A., Hikosaka, M., Rastogi, S., Toda, A., Barham, P., Goldbeck-Wood, G., *J Mater. Sci.*, 29, 2579 (1994)
15. Naumann, R.J., Introduction to the Physics and Chemistry of Materials. CRC Press, Boca Raton, FL, 2009. p279.
16. Imai, M., Kaji, K., Kanaya, T., Sakai, Y., *Phys. Rev. B*, 52, 12696 (1995)
17. Al-Hussein, M., Strobl, G., *Macromolecules*, 35, 1672 (2002)
18. Heck, B., Siegenfuhr, S., Strobl, G., Thomann, R., *Polymer*, 48, 1352 (2007)
19. Marand, H., Huang, Z., *Macromolecules*, 37, 6492 (2004)
20. Hsiao, B.S., Wang, Z.G., Yeh, F., Gao, Y., Sheth, K., *Polymer*, 40, 3515 (1999)

21. Hild, S., Boger, A., Troll, C., Rieger, B., *Polym. J*., 41, 993 (2009)

22. Hoffman, J.D. and Weeks, J.J., *J. Chem. Phys.*, 42, 4301 (1965)

23. Wunderlich, B., Macromolecular Physics, Vol 2. Academic Press, New York, 168-178 (1976)

24. Alfonso, G.C., Pedemonte, E., and Ponzetti, L., *Polymer*, 20, 104 (1979)

25. Di Lorenzo, M.L., Pyda, M., Wunderlich, B., *J. Polym. Sci. Part B: Polym. Phys. Ed.*, 39, 2969 (2001)

26. Ivanov, D.A., Hocquet, S., Dosière, M., Koch, M.H.J., *Eur. Phys. J. E.*, 13, 363 (2004)

27. Marand, H., Alizadeh, A., Farmer, R., Desai, R., Velikov, V., *Macromolecules*, 33, 3392 (2000)

28. Alizadeh, A., Richardson, L., Xu, J., McCartney, S., Marand, H., *Macromolecules*, 32, 6221 (1999)

29. Iler, H.D., "A Study of the Crystallization Kinetics of Isotactic Polystyrene". Ph.D. Dissertation, Virginia Tech (1995)

30. Cline, J., USA. NIST. Measurement Services Division and Ceramics Division. *NIST Certificate Standard Reference Material 640d*. Gaithersburg: NIST, 2010. Web. 10 Sept. 2012. https://www-s.nist.gov/srmors/view_cert.cfm?srm=640D

31. Ungár, T. "Warren-Averbach Applications." Industrial Applications of X-ray Diffraction. New York: CRC. 847-867 (2000)

32. Huang, T.C., Toraya, H., Blanton, T.N., Wu, Y., *J. Appl. Cryst.*, 26, 180 (1993)

33. Warren, B.E., X-Ray Diffraction, 1st ed., Addison-Wesley Publishing Company, Reading, MA, 1969

34. Stokes, A.R., *Proc. Phys. Soc.*, 61, (1948)

35. Jones, F.W., *Proc. Roy. Soc. A*, 166, 16, (1938)

36. Shull, C.G., *Phys. Rev.*, 70, 679, (1946)

37. Balzar, D. *Voigt Function Model in Diffraction-Line Broadening Analysis*. Defect and Microstructure Analysis by Diffraction, 1st ed., Oxford University Press, New York, 1999

38. Rigaku Corp, Integrated X-ray Powder Diffraction Software PDXL 2.0: Rietveld User Manual, 1st ed., Rigaku Corporation, Tokyo, Japan, 2010

39. Buchanan D.R., Miller, R.L., *J. Appl. Phys*., 37, 11, 4003 (1966)

40. Crist, B., Cohen J.B., *J. Polym Sci: Polym Phys Ed.*, 17, 1001 (1979)

41. Tian, H.H., Atzmon, M., *Philosophical Mag A*, 79, 8, 1769 (1999)

42. Krivoglaz, M.A., X-Ray and Neutron Diffraction in Nonideal Crystals, Springer-Verlag, Berlin, 1996, 357-420.

43. Trinkaus, H., *Phys. Stat. Sol.: B*, 51, 307 (1972)

44. Noyan, I.C., Cohen J.B., Residual Stresses, Springer, NY, 1987, p117

45. Gleiter, H. *Progr. Mater. Sci*., 33. 223 (1989)

46. Iida, S., Larson, B.C., Tischler, J., *J. Mater. Res.*, 3, 267 (1988)

47. Bor, T.C., Delhez, R., Mittemeijer, E.J., Van der Giessen, E., *Mat. Sci. Eng.*, A234-236, 896 (1997)

48. Kaganer, V.M., Koehler, R., Schmidbauer, M., Opitz, R., *Phys. Rev. B*, 55, 1793 (1997)

49. Warren, B.E., *Acta Cryst*., 8, 483 (1955)

50. Warren, B.E., *Prog. Metal. Phys*., 8, 147 (1959)

51. Stokes, A.R., Wilson A.J.C., *Proc. Camb. Phil. Soc*., 38, 313 (1942)

52. Warren, B.E., Averbach, *J. Appl. Phys.*, 23, 497 (1952)

53. Sondow, Jonathan and Weisstein, Eric W. "Harmonic Number." From *MathWorld*--A Wolfram Web Resource. http://mathworld.wolfram.com/HarmonicNumber.html

54. Roe, R.J., Methods of X-ray and Neutron Scattering in Polymer Science, 1st ed., Oxford University Press, Inc., New York, NY, 2000, p155-204

55. Kortleve, G., Tuijnman, C.A.F., Vonk, C.G., *J. Polym. Sci:A2*, 10, 123 (1972)

56. Koberstein, J.T., Morra, B., Stein, R.S., *J. Appl. Cryst.* 13, 34 (1980)

57. Ruland, W., *J. Appl. Crys.*, 4, 70 (1971)

58. Marand, H., personal communication

59. Vonk C.G., Kortleve, G., *Colloid and Polym. Sci.*, 220, 19 (1967)

60. Cser, F., *J. Appl. Polym. Sci.*, 80, 2300 (2001)

61. Ratta, V. "Crystallization, Morphology, Thermal Stability and Adhesive Properties of Novel High Performance Semicrystalline Polyimides". Ph.D. Dissertation, Virginia Tech (1999)

62. Hoffman, J.D., Miller, R.L., Marand, H., Roitman, D.B., *Macromolecules*, 25, 2221 (1992)

63. Brandrup, J., Immergut, E.H., Grulke, E.A., Polymer Handbook, 4th ed., John Wiley & Sons, Inc., New York, NY, 1999, pV91

64. Alizadeh, A., Sohn, S., Quinn, J., Marand, H., Shank, L., Iler, D., *Macromolecules*, 34, 4066 (2001)

65. Marand, H., Alizadeh, A., Sohn, S., Xu, J., Farmer, R., Prabhu, V., Cronin, S., Velikov, V., *Proc. SPE ANTEC 59*, 2, 1856 (2001)

66. Lemstra, P.J., Schouten, A.J., Challa, G., *J. Polym. Sci. Polym. Phys. Ed.*, 12, 1565 (1974)

67. Minakov, A.A., Mordvintsev, D.A., Tol, R., Schick, C., *Thermochimica Acta* 442, 25 (2006)

68. A.A. Minakov, D.A. Mordvintsev, C. Schick, *Polymer*, 45, 3755 (2004)

69. A.A. Minakov, D.A. Mordvintsev, C. Schick, *Faraday Discuss*, Self-Organizing Polymers 128, 270 (2005)

70. Liu, T., Petermann, J., *Polymer*, 42, 6453 (2001)

71. Wang, Z.G., Hsiao, B.S., Sauer, B.B., Kampert, W.G., *Polymer*, 40, 4615 (1999)

72. Albrecht, T., Strobl, G., *Macromolecules*, 28, 5827 (1995)

APPENDICES

Appendix A-SAXS Film Thicknesses and Transmission Ratios

165°C	**Average (mm)**	**Variance (mm)**	**Transmission**
10hr	0.0535	0.00055	0.804
40hr	0.0544	0.00055	0.796
175°C	**Average (mm)**	**Variance (mm)**	**Transmission**
10hr	0.0554	0.00055	0.772
40hr	0.0508	0.00045	0.800
200°C	**Average (mm)**	**Variance (mm)**	**Transmission**
10hr	0.0516	0.00055	0.808
40hr	0.0508	0.00045	0.783
212°C	**Average (mm)**	**Variance (mm)**	**Transmission**
10hr	0.0572	0.00045	0.843
40hr	0.05	0	0.798
216°C	**Average (mm)**	**Variance (mm)**	**Transmission**
10hr	0.053	0	0.843
40hr	0.0562	0.00084	0.831
219°C	**Average (mm)**	**Variance (mm)**	**Transmission**
10hr	0.0516	0.00055	0.777
40hr	0.0518	0.00045	0.828

Appendix B-Miniflex Pattern of NIST SRM 640D

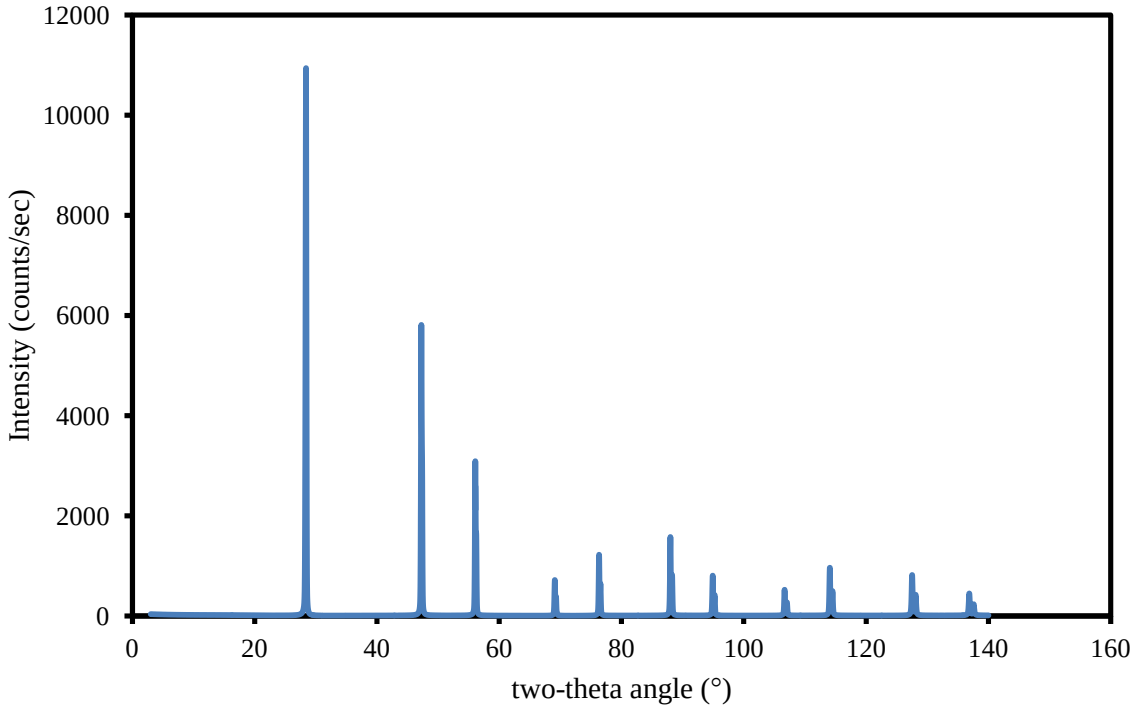

Appendix C-XRD Peak Listing from NIST SRM 640D

Information Values for Peak Positions Computed for SRM 640d Using Cu Kα Radiation, λ = 0.154 059 29 nm

h	k	l	2θ, degrees
1	1	1	28.441
2	2	0	47.300
3	1	1	56.119
4	0	0	69.126
3	3	1	76.371
4	2	2	88.024
5	1	1	94.946
4	4	0	106.700
5	3	1	114.082
6	2	0	127.532
5	3	3	136.877

Appendix D-Overlayed DSC Heating Traces

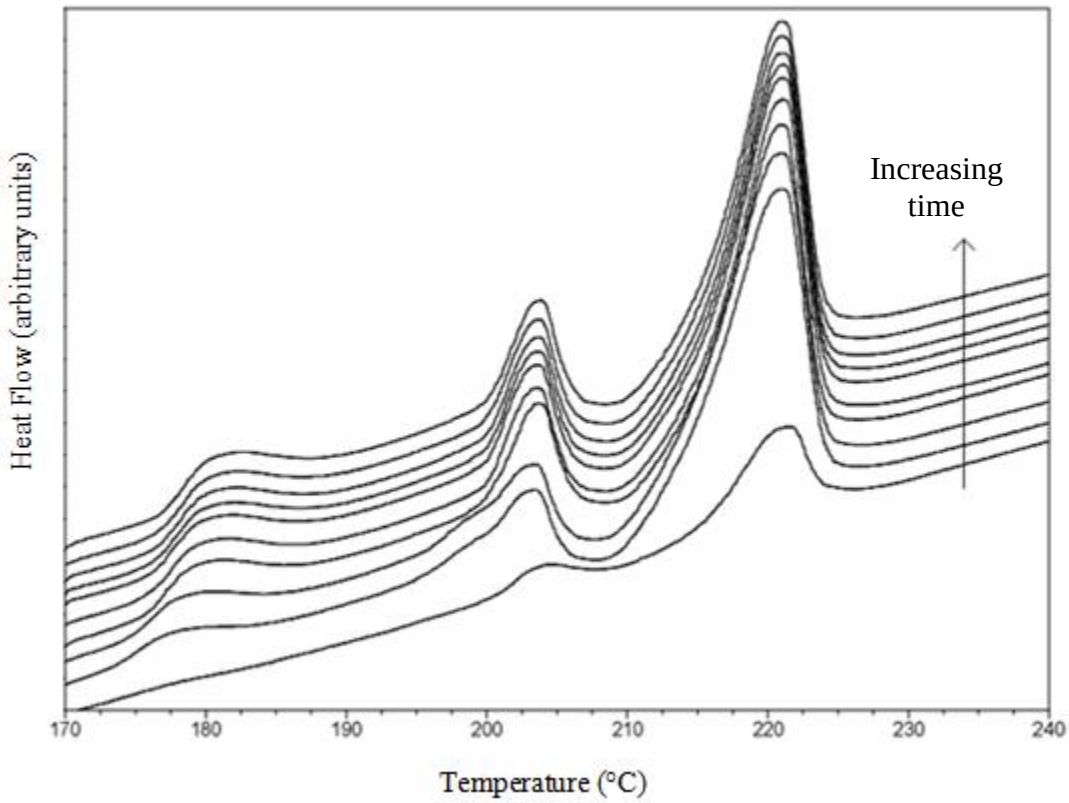

Overlay of melting experiments from it-PS isothermally crystallized at 167.3°C for varying crystallization times, from bottom to top, 1 hr, 2 hrs, 4 hrs, 10 hrs, 15 hrs, 20 hrs, 25 hrs, 25 hrs, 30 hrs, 35 hrs, 40 hrs

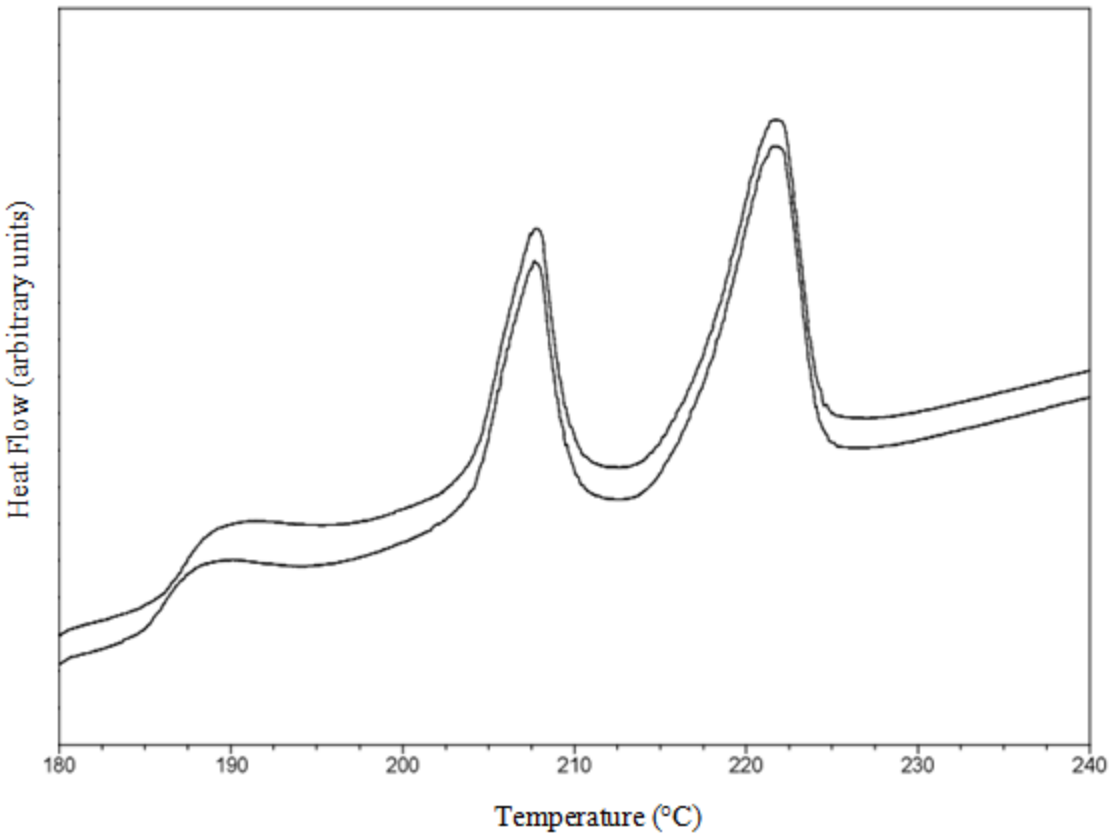

Overlay of melting experiments from it-PS isothermally crystallized at 177.4°C for varying crystallization times, from bottom to top, 10 hrs and 40 hrs

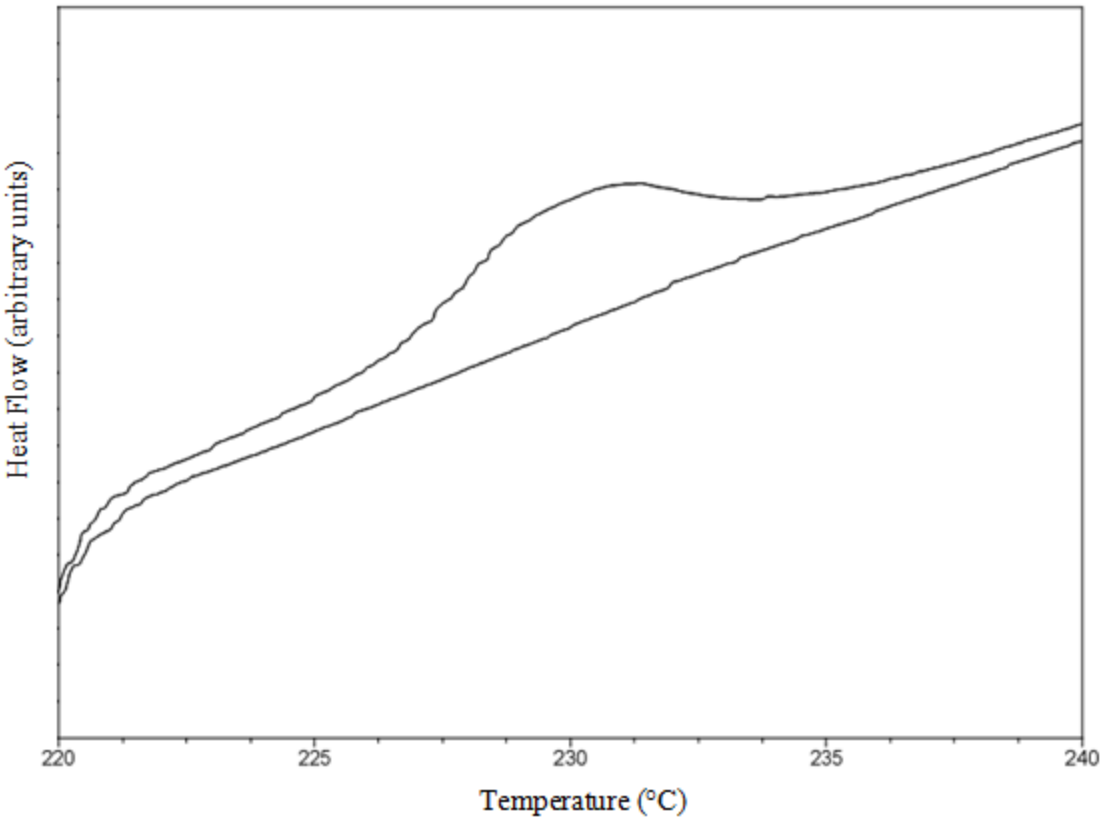

Overlay of melting experiments from it-PS isothermally crystallized at 218.6°C for varying crystallization times, from bottom to top, 10 hrs and 40 hrs

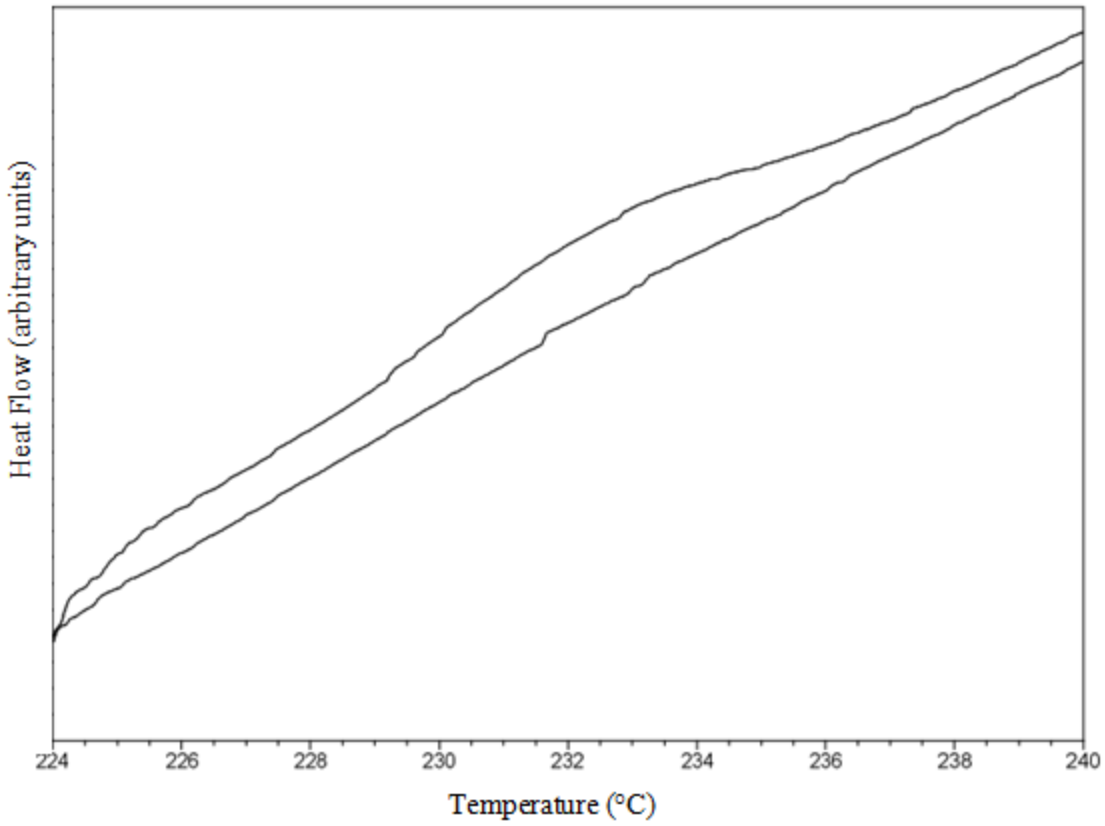

Overlay of melting experiments from it-PS isothermally crystallized at 221.7°C for varying crystallization times, from bottom to top, 10 hrs and 40 hrs